ORNL/TM-2023/2879

WIRE-21 Experiment Irradiation Conditions and In-Situ Data Collection

Christian M. Petrie
Daniel C. Sweeney
Padhraic L. Mulligan
Kara Godsey
N. Dianne B. Ezell
Paul Sirianni
Shawn Stafford
Jeff Arndt
Jorge Carvajal

April 2023

OAK RIDGE National Laboratory

ORNL IS MANAGED BY UT-BATTELLE LLC FOR THE US DEPARTMENT OF ENERGY

DOCUMENT AVAILABILITY

Reports produced after January 1, 1996, are generally available free via OSTI.GOV.

Website www.osti.gov

Reports produced before January 1, 1996, may be purchased by members of the public from the following source:

National Technical Information Service
5285 Port Royal Road
Springfield, VA 22161
Telephone 703-605-6000 (1-800-553-6847)
TDD 703-487-4639
Fax 703-605-6900
E-mail info@ntis.gov
Website http://classic.ntis.gov/

Reports are available to US Department of Energy (DOE) employees, DOE contractors, Energy Technology Data Exchange representatives, and International Nuclear Information System representatives from the following source:

Office of Scientific and Technical Information
PO Box 62
Oak Ridge, TN 37831
Telephone 865-576-8401
Fax 865-576-5728
E-mail reports@osti.gov
Website https://www.osti.gov/

ORNL/TM-2023/2879

Nuclear Science User Facilities Program

WIRE-21 EXPERIMENT IRRADIATION CONDITIONS AND IN-SITU DATA COLLECTION

Christian M. Petrie
Daniel C. Sweeney
Padhraic L. Mulligan
Kara Godsey
N. Dianne B. Ezell
Paul Sirianni
Shawn Stafford
Jeff Arndt
Jorge Carvajal

April 2023

Milestone #: M3UA-22OR0708012

Prepared by
OAK RIDGE NATIONAL LABORATORY
Oak Ridge, TN 37831
managed by
UT-BATTELLE LLC
for the
US DEPARTMENT OF ENERGY
under contract DE-AC05-00OR22725

CONTENTS

LIST OF FIGURES

LIST OF TABLES

ACKNOWLEDGMENTS

This research was sponsored by the Nuclear Science User Facilities Program of the US Department of Energy (DOE) Office of Nuclear Energy. The report was authored by UT-Battelle under contract no. DE-AC05-00OR22725 with DOE. Neutron irradiation in HFIR was made possible by the US DOE Office of Science. Kory Linton served as the program manager for this award, which is led by Westinghouse Electric Company. Adam James of Oak Ridge National Laboratory (ORNL) assisted with the initial data collection. Many others contributed to the successful design, assembly, installation, and execution of the experiment, including Shay Chapel, David Bryant, Bob Sitterson, Kurt Smith, and Maureen Searles.

ABSTRACT

This report summarizes the in situ data collected during three cycles of irradiation (~75 days) of the Wireless Instrumented Removable Beryllium Experiment 2021 (WIRE-21) in the removable beryllium (RB) positions of the High Flux Isotope Reactor (HFIR). The experiment was designed primarily to evaluate the effects of high neutron flux and fluence on the performance of wireless temperature and pressure sensors being developed by Westinghouse Electric Company (WEC). WEC's sensors could provide critical data regarding the evolution of centerline temperatures and pressurization due to fission gas release during fuel operation in light-water reactors (LWRs) or various advanced reactor applications. In addition to WEC's wireless sensors, many other sensors were interrogated, including thermocouples, self-powered neutron detectors (SPNDs), distributed fiber optic temperature sensors, and passive neutron flux wires and silicon carbide thermometry.

WIRE-21 was irradiated for a total of 75 effective full-power days over five full or partial HFIR cycles, resulting in maximum thermal and fast neutron fluences of 5.8×10^{21} and 3.4×10^{21} n/cm^2, respectively. Although two exposed thermocouples located inside WEC's sensors failed during the first irradiation cycle, the remaining 10 thermocouples that were functional at the start of the irradiation survived for the entire duration of the experiment. Measured temperatures were within the range of typical LWR operating conditions: most thermocouples reading in the ~300–400°C range. The four SPNDs all showed a measurable response to changes in reactor power, but each SPND responded differently. The fiber optic sensors show interesting evolutions in reflected signal intensities that depend significantly on the fiber dopants, type of fiber Bragg gratings (FBGs), and the light guiding mechanism (total internal reflection vs. photonic band gap). The discrepancies in the SPND data and the detailed evolution of the fiber optic sensors are being investigated by the Advanced Sensors and Instrumentation program of the US Department of Energy, Office of Nuclear Energy.

Multiple temperature and pressure transients were actuated to compare the response of WEC's sensors with reference thermocouples or ex-core pressure transducers, respectively. WEC's sensors successfully captured all actuated temperature transients, even after accumulating fast neutron fluence on the order of 2×10^{21} n/cm^2. Significant reductions in the inductance in WEC's six inductors caused some drift in the wireless sensors. These effects appear to be related to rate effects (i.e., higher neutron flux), as they were not observed during previous testing at lower neutron flux. However, WEC's temperature sensor remained functional even after the inductances decreased. Unfortunately, WEC's pressure sensor showed no response during pressurization of the metal bellows. Post-irradiation examination will help inform why the sensor did not respond to changes in applied pressure and determine the mechanism for the decrease in inductances.

1. INTRODUCTION

The successful deployment of new sensor technologies in nuclear reactors requires demonstrating acceptable performance in a representative environment. For in-core sensors, this demonstration process typically requires access to experimental test reactors that can simulate the intended operating conditions for the targeted reactor application. For relatively new sensor technologies with low technology readiness levels, testing in relatively low-power university test reactors is a logical starting point before embarking on more complex, expensive testing in high-power research reactors. As a particular sensor technology progresses in its technological readiness level and demonstrates successful performance during experiments at relatively low neutron flux, the case can be made that the sensor is ready for more prototypic testing.

Westinghouse Electric Company (WEC) followed this general approach in their development of wireless sensors for monitoring the centerline temperature and internal pressure of light-water reactor (LWR) fuel rods. The motivation for this sensor development was to collect valuable in situ data during neutron irradiation of advanced fuel technologies in the form of lead test rods or lead test assemblies in commercial LWRs. If successful, these sensors could provide significantly more data than it would be possible to collect from either post-irradiation examination (PIE) or a limited set of in situ data collected in test reactors during the fuel qualification process. This wealth of data would support the licensing case for the fuel without risking fuel rod failure caused by penetrations that would otherwise be required to route sensor leads through the pressure boundary of the fuel rod. This effort is a part of a larger initiative across the nuclear industry to accelerate the fuel qualification process by leveraging recent advances in modeling and simulation, separate effects irradiation capabilities, and in situ data collection [1].

WEC performed initial testing of wireless sensors based on inductive coupling in the Penn State Breazeale Reactor before progressing to testing at a higher neutron flux within the pressurized water loop facilities in the Massachusetts Institute of Technology Reactor (MITR) [2, 3]. The final step in their sensor development effort was to test at even higher neutron flux levels that would allow the sensors to approach end-of-life neutron fluence levels in a reasonable amount of time. The removable beryllium (RB) positions of the High Flux Isotope Reactor (HFIR) at Oak Ridge National Laboratory (ORNL) were selected for this testing because of their extremely high neutron flux: $\sim 5 \times 10^{14}$ n/cm^2/s for neutron energies > 0.1 MeV and $\sim 10^{15}$ n/cm^2/s for neutron energies < 1 eV. WEC proposed conducting irradiation of their wireless sensor technologies to the US Department of Energy, Office of Nuclear Energy, through the Nuclear Science User Facilities program, which provides users with access to the unique facilities available at the US national laboratories and other partner facilities. After the proposal was awarded, a novel irradiation vehicle was designed to accommodate WEC's sensors, test them under the desired neutron flux and temperature conditions, and independently actuate their temperature and pressure sensors remotely [4].

The Wireless Instrumented RB Experiment 2021 (WIRE-21) was assembled, delivered to HFIR, and inserted during HFIR cycle 498 in April 2022 [5]. WIRE-21 is the most highly instrumented experiment ever performed in HFIR's >60 year operating history. This report summarizes the experiment operating conditions and the in situ data collected during operation of three HFIR cycles for approximately 75 effective full-power days.

2. METHODS

2.1 EXPERIMENT CONFIGURATION

Figure 1 shows a layout (not to scale) of the instrumentation included in the WIRE-21 experiment. WEC's temperature sensor was located closer to the reactor midplane, where nuclear heating rates were higher and could drive higher internal temperatures meant to simulate LWR fuel operating conditions (i.e., ~600–1000°C). WEC's pressure sensor was located farther from the core midplane, where the nuclear heating rates were lower, so that the temperatures would be closer to LWR coolant temperatures (i.e., ~300°C). A helium purge gas line (P) terminated at the bottom of the experiment and provided the primary gas flow from the bottom to the top of the experiment, where an additional gas line was located to carry the effluent gases out to HFIR's hot off-gas monitoring system. Two control gas lines (G) terminated below the holders containing WEC's temperature and pressure sensors. These gas lines allowed for locally varying the He and Ar content to change the local thermal conductivity of the gas surrounding the experiment components. Adjusting the gas conductivity changes the ability to transfer nuclear heating from the internal components to the reactor coolant, which allows for control of local experiment temperatures.

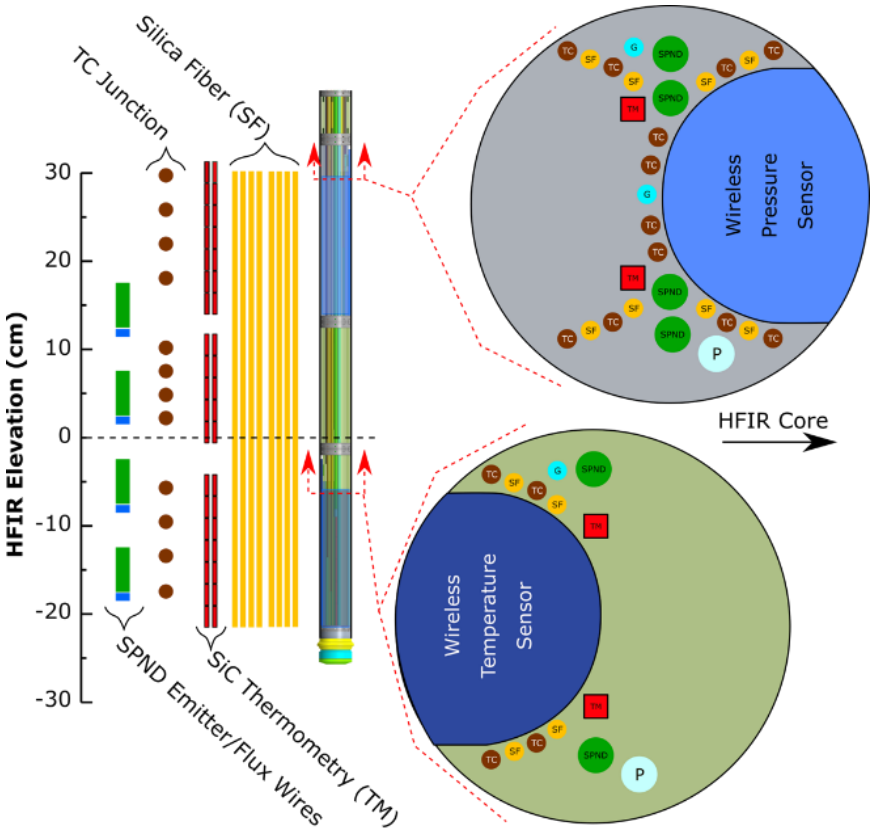

Figure 1. In-core instrumentation layout for WIRE-21 (not to scale) [6].

A total of 12 thermocouples (TCs) were included in the graphite holders of the experiment at various elevations relative to the HFIR core midplane. Two additional TCs were included inside WEC's temperature sensor and above WEC's pressure sensor. Unfortunately, these two TCs failed during the first HFIR cycle, likely because their junctions were bare and more susceptible to mechanical failure. Two of the TCs in the graphite holders were shorted during experiment installation and could not be interrogated during the test. Passive SiC temperature monitors (TMs) were located throughout the experiment so that

dilatometric measurements made post-irradiation on these samples [7] could be compared with the in situ measurements from the TCs.

Four self-powered neutron detectors (SPNDs) with V emitters were positioned at ±5 and ±15 cm from the reactor midplane. A series of metal flux wires were included near each SPND so that the integrated fluence could be determined based on neutron activation analysis of the flux wires and used to calibrate the SPND data. Finally, eight silica fiber (SF) optic sensors were included to provide spatially distributed temperature measurements and compare those data with the measurements from the TCs and passive SiC TMs.

2.2 WEC SENSOR LAYOUT AND OPERATING PRINCIPLES

Figure 2 shows the spatial profiles of the time-averaged fast (i.e., energy > 0.1 MeV) and thermal (i.e., energy < 1 eV) neutron flux for WEC's temperature sensor (TS) and pressure sensor (PS). The figure also shows models of the internals of WEC's sensors (top covers removed) and the individual inductors (Tx, Rx1, and Rx2) that were interrogated during irradiation. The markers indicate the neutron flux values in the TS (red markers) and PS (blue). The "X" markers indicate the fast neutron flux values, and the dots indicate the thermal neutron flux values. Both sensors have a variation in neutron flux moving from the bottom to the top inductor. The TS has a significantly higher ratio of thermal to fast neutron flux compared with that of the PS.

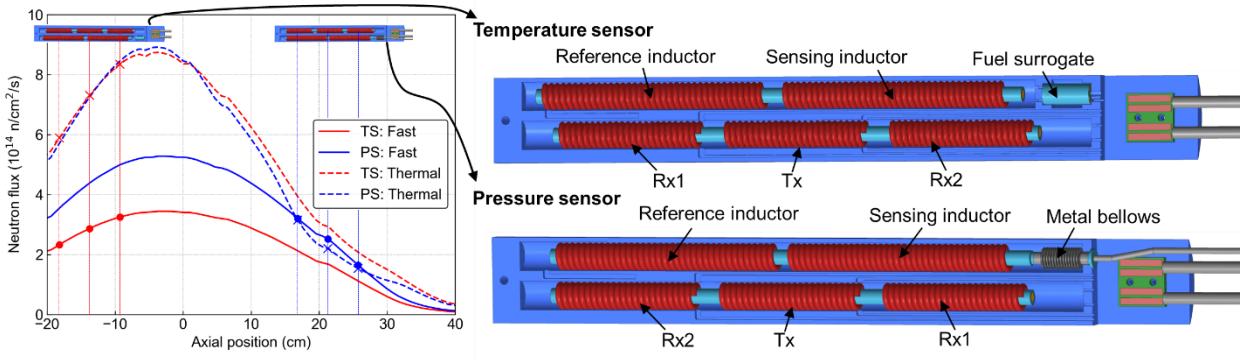

Figure 2. (Left) Spatial profiles of the time-averaged fast (energy > 0.1 MeV) and thermal (energy < 1 eV) neutron flux for WEC's temperature sensor (TS) and pressure sensor (PS). The markers indicate the neutron flux values in the TS (red markers) and PS (blue). The "X" markers indicate the fast neutron flux values, and the dots indicate the thermal neutron flux values. (Right) Models showing the internals of WEC's sensors (top covers removed) and the individual inductors (Tx, Rx1, and Rx2) that were interrogated during irradiation.

WEC's sensors operate by applying a pulse or continuous current to the transmit (Tx) inductor, which generates a time-varying magnetic field around the inductor. The passive side of the circuit comprises two inductors ("reference" and "sensing") that are positioned so that each receives an equal amount of the incident magnetic field from the transmitter coil to develop an equal voltage across each inductor. This establishes a current in each sensor coil loop, which, in turn, generates a return magnetic field that is received by transceiver receiver inductors Rx1 and Rx2. Because of the symmetry of the transceiver and sensor configurations, the voltages of each of the transceiver receiver inductors will be equal. Connecting the receiver coils in series but out of phase (or in "anti-series") causes the voltage to effectively sum to zero. The zero signal represents a "balanced" configuration, with the Rx1 and Rx2 coil loops containing equal amounts of current. When some device or process causes an imbalance in the currents developed in the Rx1 and Rx2 coil loops, the receiver coils develop a resultant voltage. In this respect, the transceiver acts like a linear variable differential transformer (LVDT).

WEC's sensors operate by introducing additional components in the passive side of the sensors to intentionally upset the balance in the currents developed in the Rx1 and Rx2 coil loops in response to a change in temperature and/or pressure. The temperature sensor operates by introducing a resistance temperature detector (RTD) in the passive sensor coil loop, which affects the current as its temperature changes. The pressure sensor includes a mechanical bellows attached to the ferritic core of the sensing inductor in the passive side of the sensor. As the bellows expands or contracts with changes in pressure, the translation of the inductor core affects the inductance of the passive circuit and the resulting electromagnetic coupling between the sensor inductor and the transceiver receiver inductor (Rx1). In the temperature and pressure sensors, reference inductors are included in the passive circuits that are either not connected to an RTD (TS) or contain a ferritic core that is not coupled to a mechanical bellows (PS). These reference inductors enable compensation for the effects of radiation or other interfering inputs that may alter the electromagnetic coupling between the transceiver circuit and passive circuit independent of the desired measurands (i.e., temperature and pressure).

WEC's PS was actuated using a static gas line that ran from the metal bellows back to the Materials Irradiation Facility (MIF), which is adjacent to HFIR. A regulator on a He cylinder was adjusted until the setpoint pressure was reached, as measured by a conventional pressure transducer located in the MIF. Pressure actuation causes the ferritic core attached to the end of the metal bellows to translate axially inside the wire wrap of the sensing inductor. WEC's TS was actuated by increasing the Ar content in the vicinity of the TS, which caused the temperatures to increase. Increasing temperatures change the resistance of the wire that was wrapped around the fuel surrogate (i.e., the RTD), which affects the inductive coupling from the sensing inductor to Rx2.

3. RESULTS

3.1 OPERATING HISTORY

Table 1 and Figure 3 show the reactor power history for the three HFIR operating cycles during which WIRE-21 was irradiated. HFIR cycles 498 and 500 were both split into two parts (e.g., 498a and 498b) with a brief outage between them. Cycle 498a ran for 10.7 effective full-power days (EFPDs) followed by an additional 14.7 EFPDs during cycle 498b. There was a long outage (i.e., >140 days) between cycles 498b and 499, which ran for 25.8 EFPDs. The outage between cycles 499 and 500a was significantly shorter (i.e., 18 days). Cycles 500a and 500b ran for 10.5 and 13.9 EFPDs, respectively. In total, WIRE-21 was irradiated for 75 EFPDs, resulting in maximum thermal and fast neutron fluences of 5.8×10^{21} and 3.4×10^{21} n/cm^2, respectively. Table 2 summarizes the thermal and fast neutron fluence for each inductor as well as the time-averaged thermal and fast neutron flux values.

Table 1. HFIR cycle history of WIRE-21

Cycle Number	Start Date	End Date	Duration (days)
498a	4/5/2022 8:38	4/16/2022 1:03	10.7
498b	4/22/2022 8:03	5/7/2022 1:55	14.7
499	9/27/2022 8:35	10/23/2022 2:59	25.8
500a	11/8/2022 9:03	11/18/2022 20:02	10.5
500b	12/2/2022 14:02	12/16/2022 12:44	13.9

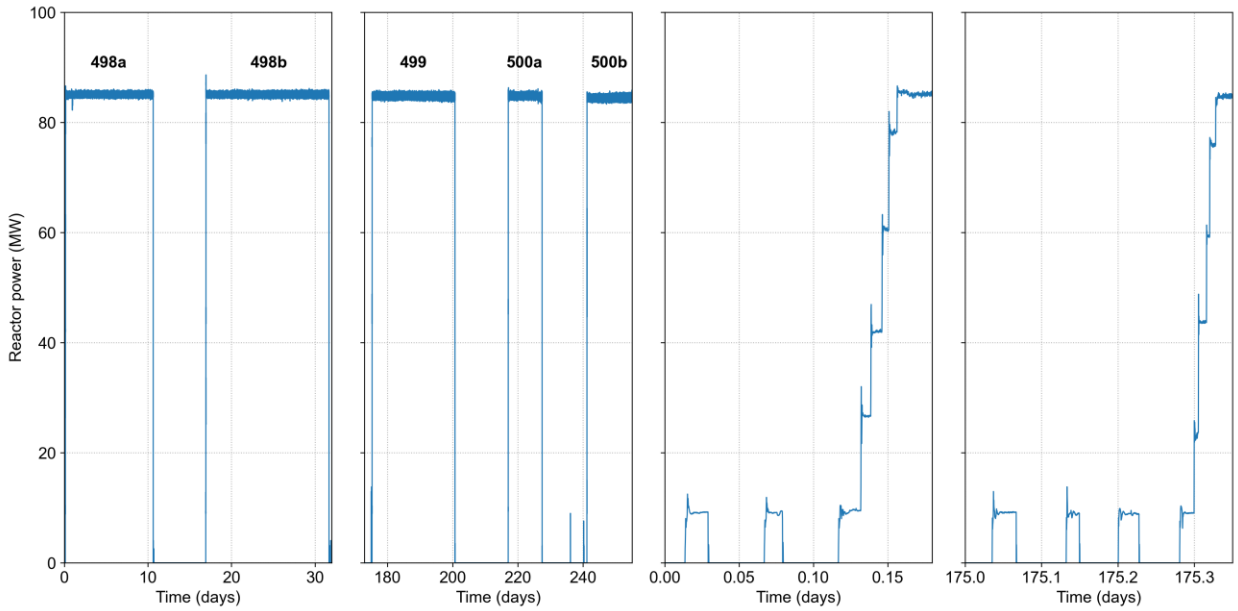

Figure 3. Evolution of reactor power history as a function of calendar days from the start of HFIR cycle 498. HFIR cycles 498, 499, and 500 are indicated. Cycles 498 and 500 were split into two parts. The two plots on the right show the startup operations for cycles 498a and 500a.

Table 2. Thermal (energy <1 eV) and fast (energy > 0.1 MeV) neutron fluences and time-averaged flux values for each inductor in WEC's temperature and pressure sensors.

Sensor	Inductor	Axial location (cm)	Thermal neutron flux (10^{14} n/cm^2/s)	Fast neutron flux (10^{14} n/cm^2/s)	Thermal neutron fluence (10^{21} n/cm^2)	Fast neutron fluence (10^{21} n/cm^2)
Temperature	Rx1	−18.19	5.9	2.3	3.8	1.5
	Tx	−13.74	7.3	2.9	4.7	1.9
	Rx2	−9.30	8.3	3.3	5.4	2.1
Pressure	Rx2	16.84	3.1	3.2	2.0	2.1
	Tx	21.29	2.2	2.5	1.4	1.6
	Rx1	25.73	1.5	1.6	1.0	1.1

3.2 TEMPERATURE HISTORY

Figure 4 summarizes the temperature history measured by the TCs located at various axial locations within the graphite holders that surround WEC's TS and PS. Results are shown as a function of EFPDs and as a function of axial position at the beginning of cycle (BOC) and end of cycle (EOC). In this figure, cycles 1, 2, and 3 refer to HFIR cycles 498, 499, and 500. Temperatures generally increase during the first cycle (~25 EFPDs), which is due to a combination of increased nuclear heating rates and radiation-induced changes in the thermophysical properties of the graphite holders.

As the HFIR control plates are withdrawn throughout a cycle, the peak fission density within the HFIR fuel shifts radially outward, which increases nuclear heating rates in the RB positions that are located radially outside the control plates. In addition, the fine-grain graphite materials used for the experiment holders are known to undergo compaction under neutron irradiation, until they eventually reach a

turnaround fluence beyond which they start to swell. Turnaround typically occurs at fast neutron fluences on the order of 10^{22} n/cm^2, which is significantly higher than the levels reached in WIRE-21. However, the dimensional changes generally decrease with increasing fluence as the fluence approaches turnaround. This is consistent with the WIRE-21 temperatures showing the most significant increases in temperature during the first irradiation cycle (498). The temperatures closer to the reactor midplane are generally more stable than those further from the midplane. This is likely because the control plate movements have a larger impact at the top and bottom of the core when the highly absorbing regions of the control plates are moved further away from the core. Finally, graphite thermal conductivity is also degraded under irradiation, which would also result in increased temperatures with increasing neutron fluence.

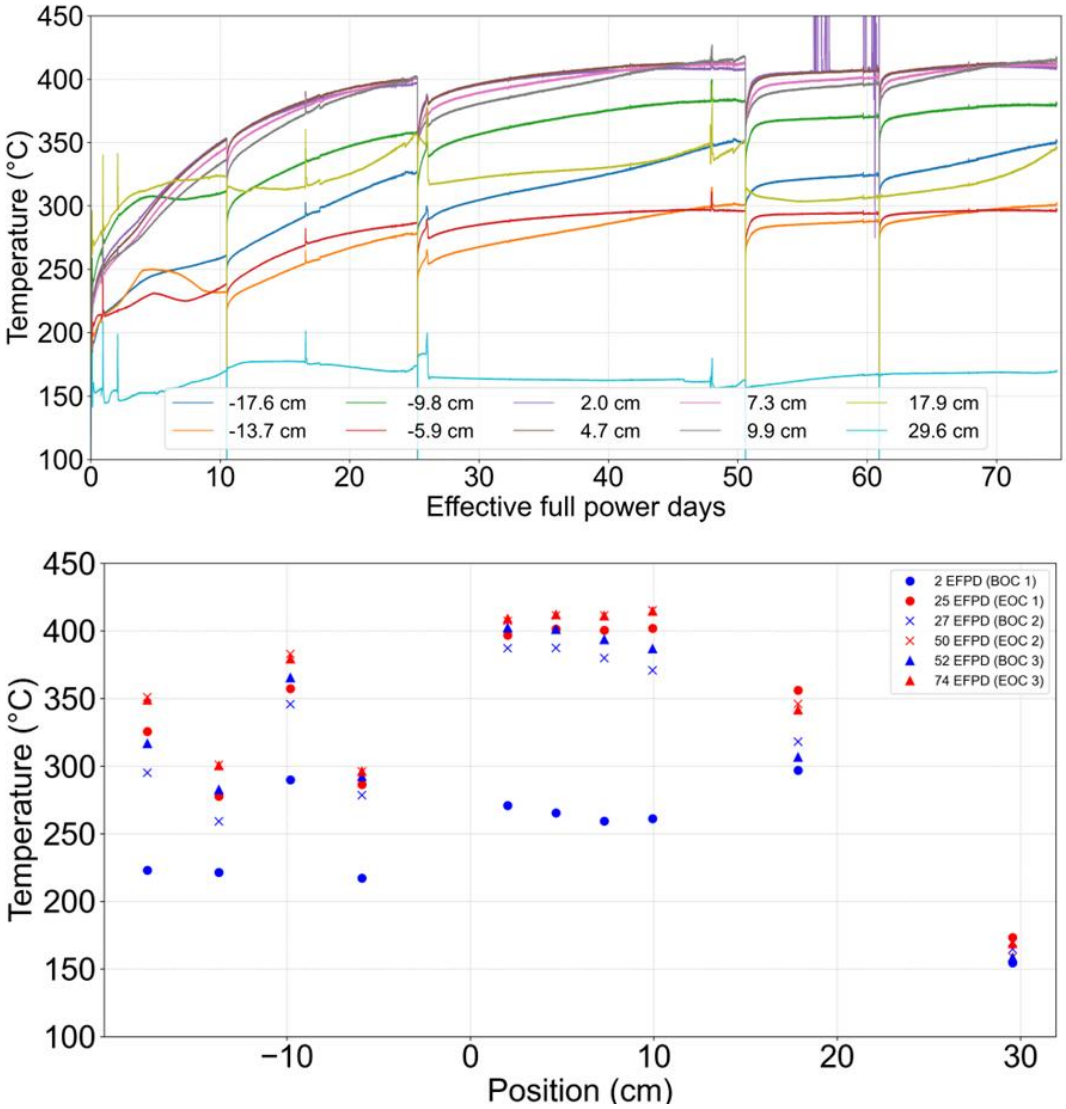

Figure 4. Temperature history of WIRE-21. (Top) Time history for thermocouples with locations relative to the core midplane indicated in the legend and (bottom) temperature profiles, relative to the core midplane, at various effective full power days (EFPDs) representing beginning-of-cycle (BOC) and end-of-cycle (EOC) conditions.

3.3 ACTUATED TEMPERATURE AND PRESSURE TRANSIENTS

In addition to the gradual increases in temperature throughout each HFIR cycle, transient temperature changes also occur at various points throughout the irradiation. These were intentional temperature

transients actuated by adjusting the flow rates in the purge gas line and the two control gas lines mentioned in Section 2.1. Figure 5 shows the volume percentage of He and Ar surrounding the TS and PS as a function of time (EFPDs). A total of five temperature transients were run, which are shown in more detail in the bottom plots. Efforts were made to increase the temperature in the TS while minimizing the increases in temperature in the PS. This was performed by increasing Ar flow in the vicinity of the TS while increasing the He flow in the vicinity of the PS. However, because the flow travels from bottom to top, the Ar that is flowed into the TS region must also pass up through the PS, resulting in some increases in temperature near the PS. More detail regarding the local temperature measurements made during these transients is provided later in Sections 3.4 and 3.4 when discussing measurements from WEC's sensors.

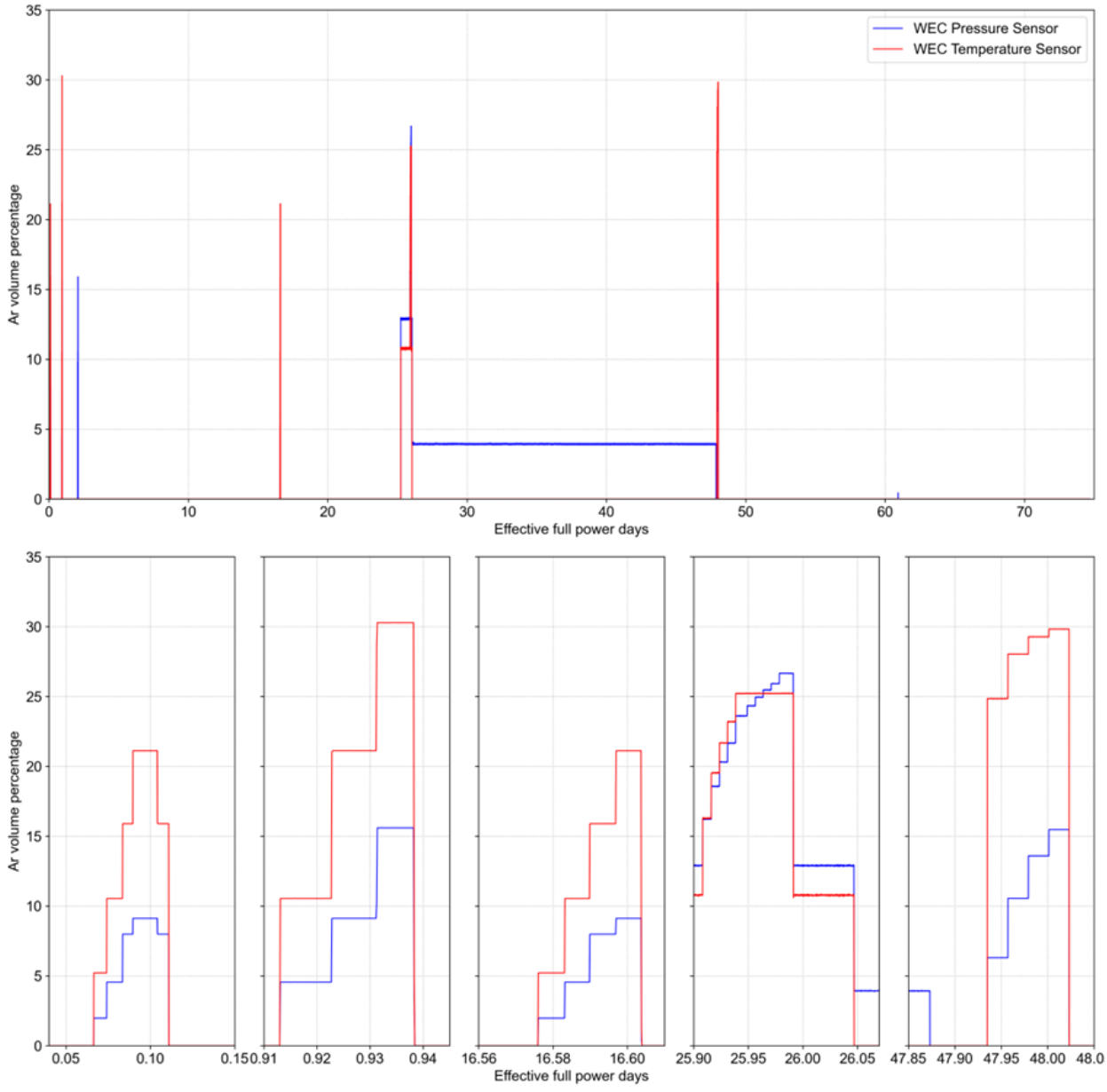

Figure 5. Evolution of gas composition surrounding WEC's temperature and pressure sensors calculated from the measured flow rates of He and a 30 mol % Ar, He balance mixture in different regions of the experiment. The top plot shows the entire operating history, and the bottom plots show individual transients.

In addition to actuating the TS by adjusting He and Ar flow rates, the PS was actuated using a regulator on a gas bottle located in the MIF that is connected to the bellows in the PS via a gas line. This static pressure was increased in steps and then decreased by venting the line in the MIF. The pressure was logged using two redundant pressure transducers located near the regulator in the MIF. Figure 6 summarizes the pressure measured in the MIF as a function of time (i.e., EFPDs). Two transients were conducted during irradiation at the beginning of HFIR cycles 498 and 499. The pressure was ramped up in steps of ~25 psi to maximum pressures of ~600 and 700 psi during HFIR cycles 498 and 499, respectively. In addition, two pressure transients (visible around 10.5 EFPDs in the left plot of Figure 6) were conducted during the outage in between cycles 498a and 498b to evaluate the PS response while the reactor was not operating. The two latter transients are not shown in detail, but the pressure was increased in steps of 50 psi to ~300 and 500 psi, respectively.

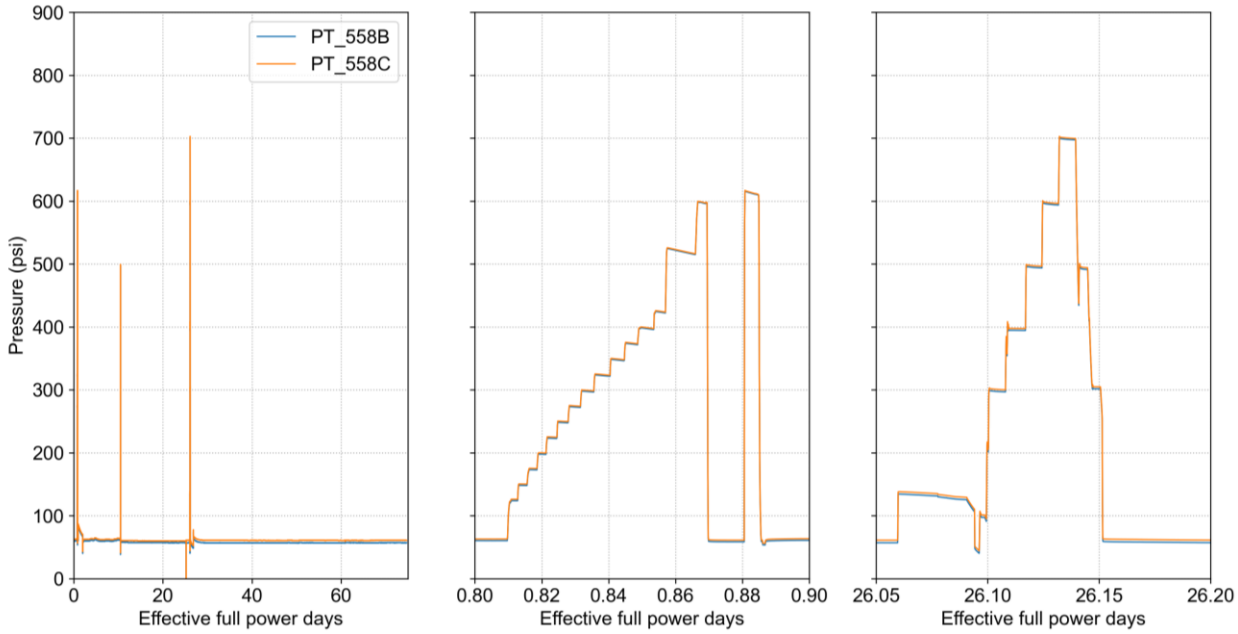

Figure 6. Measured pressure delivered to the bellows inside the WEC pressure sensor determined from two separate pressure transducers located near the gas delivery system. Results show the entire operating history (left) and the two pressure transients run at the beginning of HFIR cycles 498 and 499 (center and right, respectively).

3.4 INDUCTIVE COUPLING IN WEC SENSORS

Figure 7 shows the root mean square (RMS) voltages from WEC's temperature sensor (Rx2, red curve) and pressure sensor (Rx1, green curve) during the first ascent to full reactor power in cycle 498a. The reactor power evolution (orange curve) is plotted on the right axis. The sensor signal variation as the reactor power is increased from 12:50 PM through 1:30 PM was caused by the large thermal gradient along the length of the sensors (see simulated temperature distributions reported previously [5]). As described in Section 2.2, the sensor functionality relies on symmetry between the receiver coils. During the reactor startup, transient temperature variations in the receiver coils cause an imbalance in the signal response. As the reactor reaches full power and the temperatures reach an equilibrium, the voltages measured in the transceiver receiver inductor circuits stabilize, as shown beginning at approximately 1:32 PM.

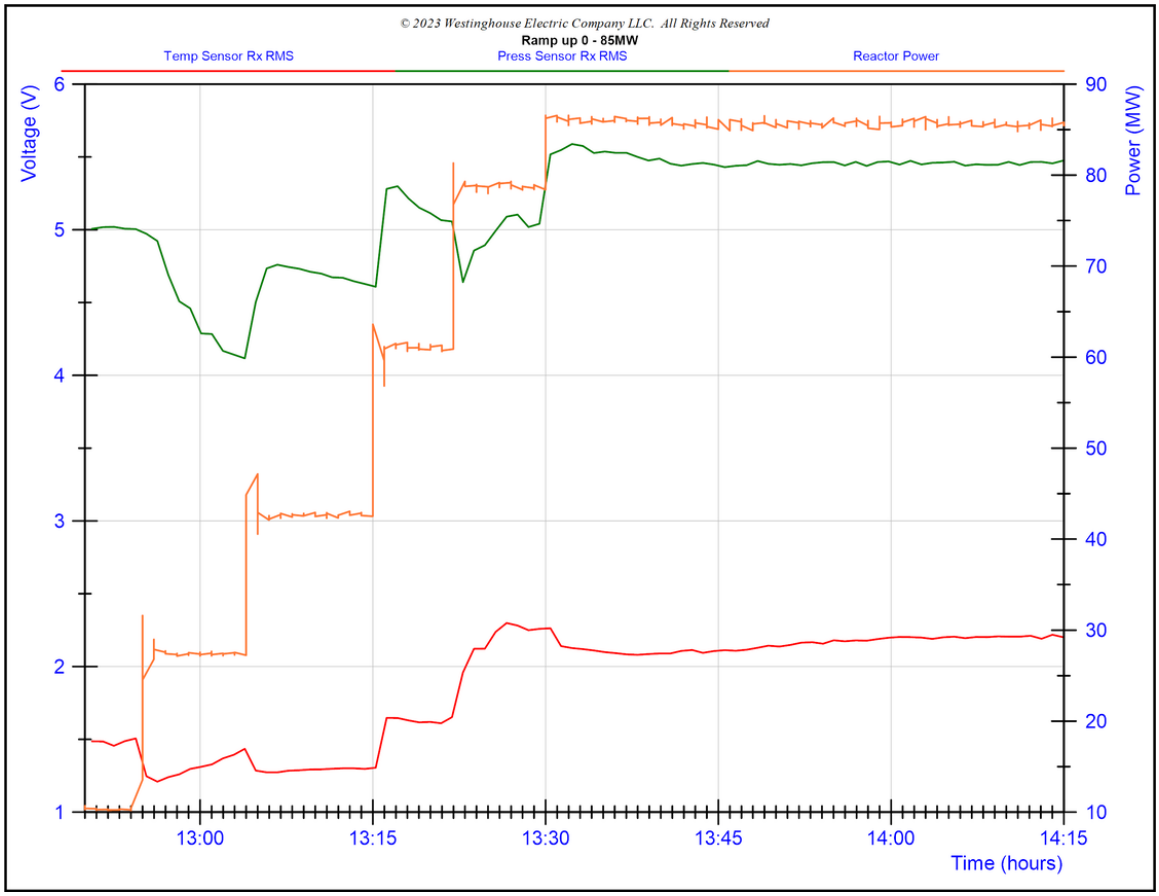

Figure 7. Time evolution of the RMS voltages measured from WEC's temperature sensor (Rx2, red curve) and pressure sensor (Rx1, green curve) during the first ascent to full reactor power on 4/5/2022 (cycle 498a). The reactor power evolution (orange curve) is plotted on the right axis.

Figure 8 shows the response of WEC's temperature and pressure sensors to the first temperature transient that was performed during the first day of full reactor power operation in cycle 498a. The gas mixtures were shown previously in the bottom left plot of Figure 5. The increases in Ar caused the temperature in the fuel surrogate to increase in steps from ~500°C to >620°C. Both sensors respond to the increases in temperature, but around 15:15 there is evidence of permeability degradation in the Rx coils (decreased inductance), which causes the RMS voltages to drift. The pressure sensor also responds to changes in temperature, potentially due to changes in material properties or dimensional changes resulting from thermal expansion of the sensor materials.

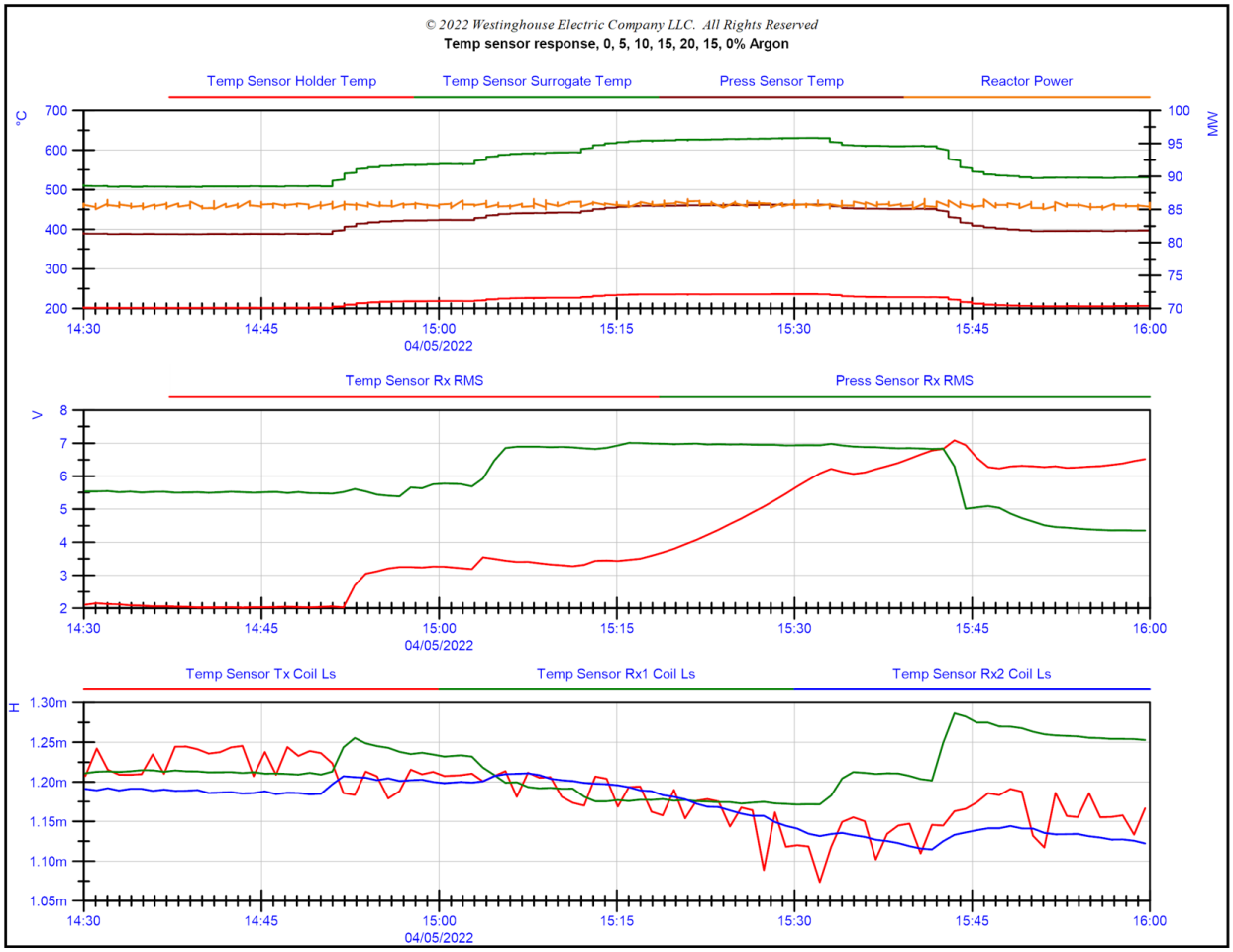

Figure 8. Top: Time evolution of the reactor power (right axis) and the temperatures (left axis) measured near WEC's sensors and in the holder surrounding WEC's temperature sensor during the first temperature transient performed during the first day of operation of cycle 498a. Middle: Time evolution of the RMS voltages measured from WEC's temperature sensor (Rx2, red curve) and pressure sensor (Rx1, green curve). Bottom: Time evolution of the inductances measured in the three inductors in the transceiver circuit of WEC's temperature sensor.

Although there appears to be evidence of drift in WEC's temperature sensor early in the first cycle, the sensor appears to stabilize later in the test. Figure 9 shows the response of WEC's temperature sensor to the final temperature transient performed toward the end of cycle 499. The gas mixtures were shown previously in the bottom right plot of Figure 5. The increases in Ar caused the temperature in the fuel surrogate to increase in steps from ~550°C to 650°C. The sensor responds accordingly as shown by the middle plot, in which RMS voltages increase from approximately 350 mV to 700 mV and then decrease after the transient is complete.

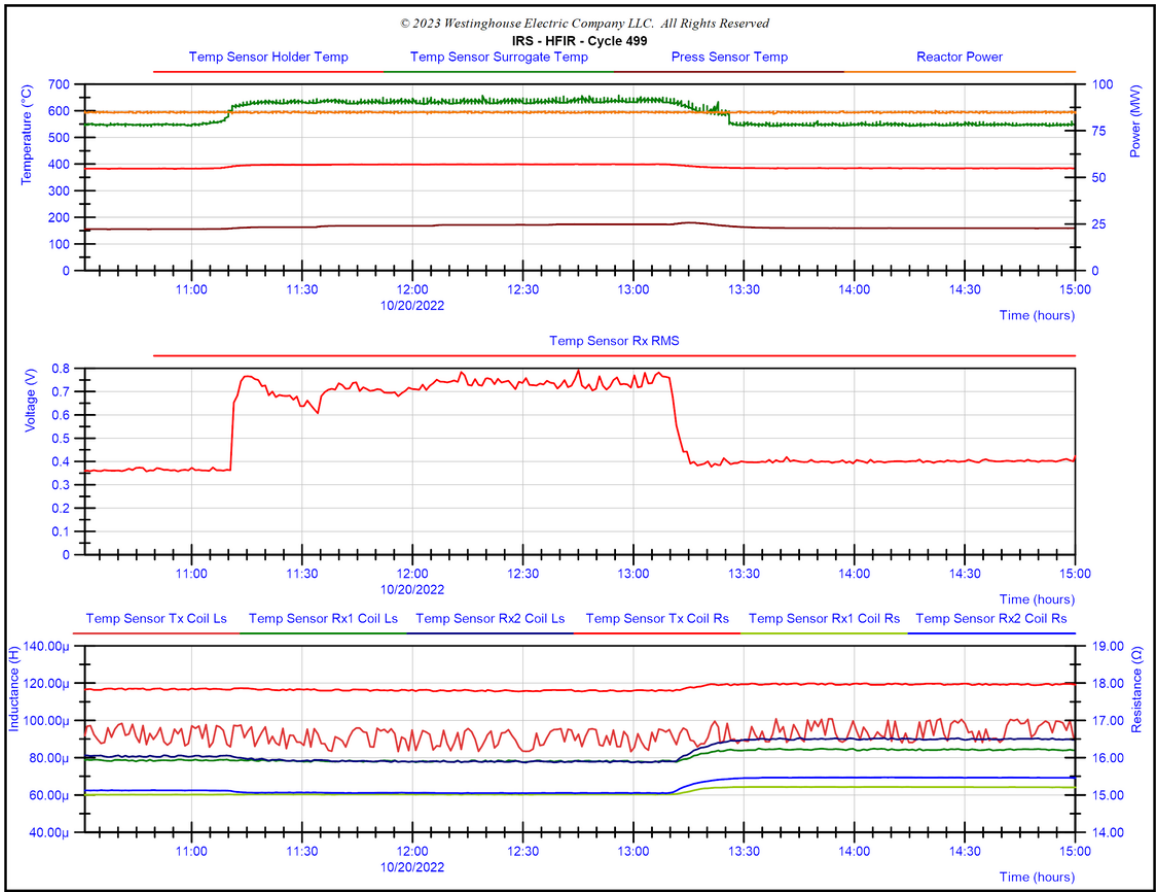

Figure 9. Top: Time evolution of the reactor power (right axis) and the temperatures (left axis) measured near WEC's sensors and in the holder surrounding WEC's temperature sensor during the final temperature transient performed toward the end of cycle 499. Middle: Time evolution of the RMS voltages measured from WEC's temperature sensor. Bottom: Time evolution of the inductances and resistances measured in the three inductors in the transceiver circuit of WEC's temperature sensor.

Unfortunately, WEC's pressure sensor showed no response during pressurization of the metal bellows. The same sensor was tested prior to irradiation and was shown to respond when the bellows was pressurized. It is possible that some mechanical interference or flow obstruction occurred during experiment assembly that might have affected the bellows' deformation or the ability of the ferritic core to translate inside the sensor enclosure. PIE will help inform why the sensor did not respond to changes in applied pressure.

3.5 EVOLUTION OF WEC SENSOR ELECTRICAL PROPERTIES

Some additional insight into WEC's sensor operation can be gained by evaluating changes in the resistances and inductances of the transceiver coil circuits over the course of the irradiation. Figure 10 shows the inductance and resistance of the inductor circuits in WEC's temperature sensor vs. fast neutron fluence in the early periods of the irradiation. The temperatures nearest each inductor (sensor IDs indicated in the figure legend) are also plotted on the right axes as a function of neutron fluence. The changes in resistance were relatively minor. However, the inductances decreased significantly (by more than a factor of 5 in some cases), and the decreases were more significant in the inductors that were exposed to a higher neutron flux. For example, Rx2 is located closest to the reactor core midplane (highest neutron flux), followed by Tx and Rx1. Interestingly, Rx1 (lowest neutron flux) shows no significant reductions in inductance for fast neutron fluences up to 10^{19} n/cm^2, whereas significant

reductions in inductance were observed in the Tx and Rx2 inductors at the same neutron fluence. Therefore, the reductions in inductance appear to be related to neutron flux and not neutron fluence (i.e., a rate effect). Further supporting this theory is the fact that these reductions in inductance were not observed previously during irradiation testing at lower neutron flux in MITR [3]. The large reductions in inductance appear to have no correlation with changes in local temperature.

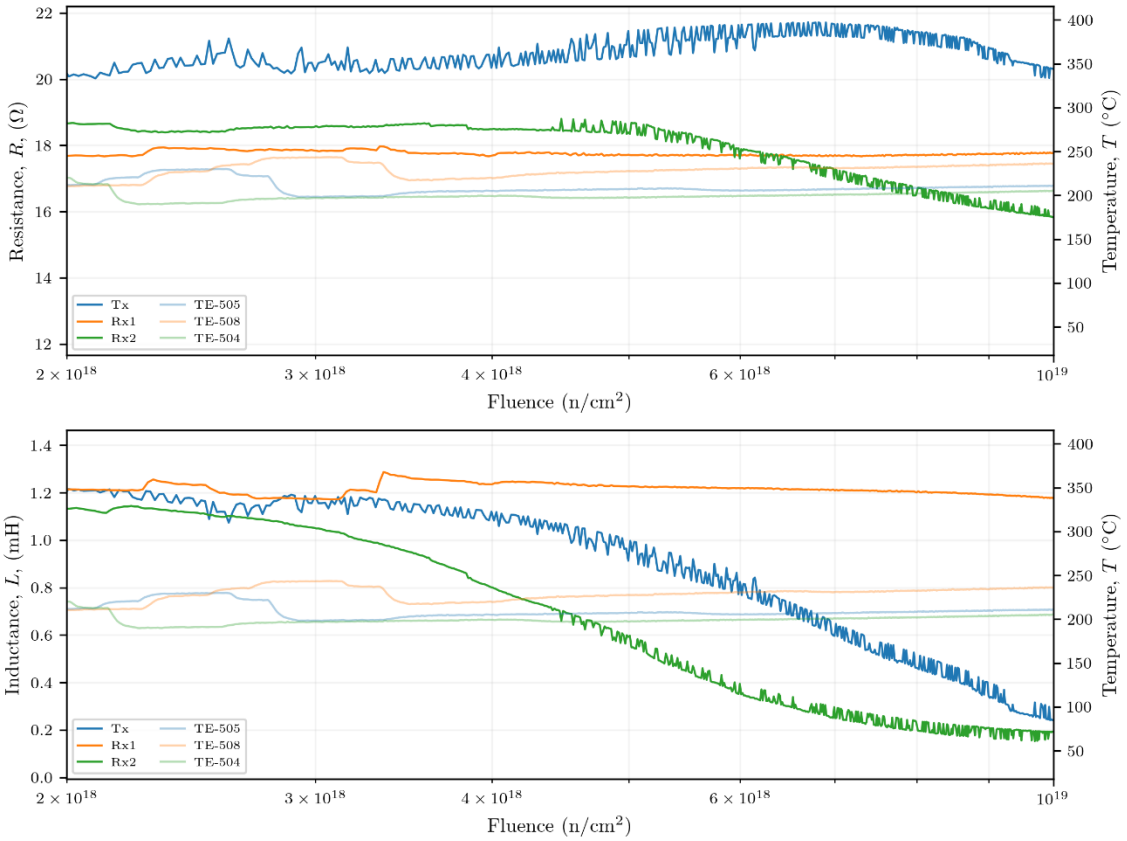

Figure 10. Change in the resistance (top) and inductance (bottom) of the three inductor circuits in WEC's temperature sensor vs. fast neutron fluence in the early periods of the irradiation. The temperatures nearest each inductor (sensor IDs indicated in the figure legend) are also plotted on the right axes as a function of neutron fluence.

Figure 10 through Figure 14 show the inductance and resistance of the inductor circuits in WEC's temperature and pressure sensors vs. fast neutron fluence (on a linear scale) throughout HFIR cycles 498 and 499. The temperatures nearest each inductor (sensor IDs indicated in the figure legend) are also plotted on the right axes as a function of neutron fluence. Like the data shown previously at lower neutron fluence, the resistances are not significantly affected even at a higher neutron fluence. The large reductions in inductance that occur at lower neutron fluence generally reach an equilibrium near ~0.1–0.2 mH, except for the Rx1 inductor in the pressure sensor, which approaches an equilibrium value of ~0.6–0.7 mH. The higher inductance in this inductor could be a result of this inductor being irradiated at the lowest fast neutron flux (see Table 2).

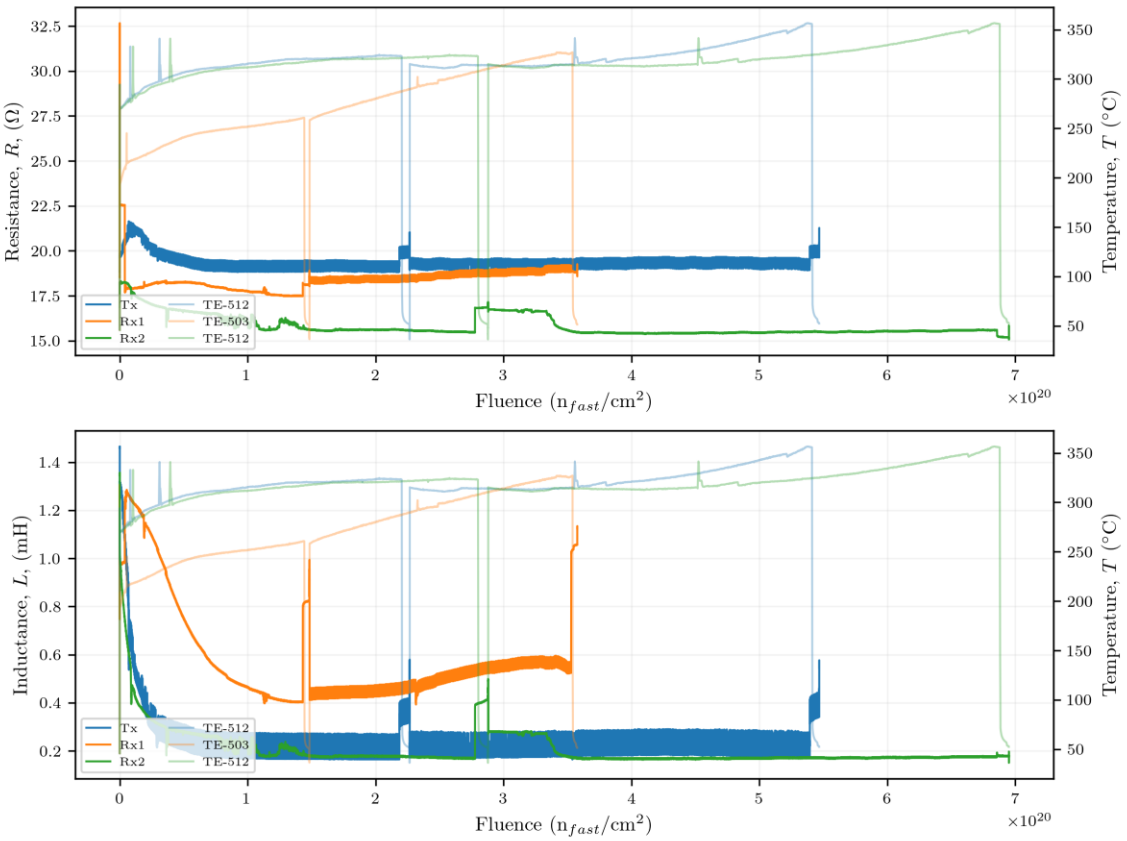

Figure 11. Change in the resistance (top) and inductance (bottom) of the three inductor circuits in WEC's pressure sensor vs. fast neutron fluence during cycle 498. The temperatures nearest each inductor (sensor IDs indicated in the figure legend) are also plotted on the right axes as a function of neutron fluence.

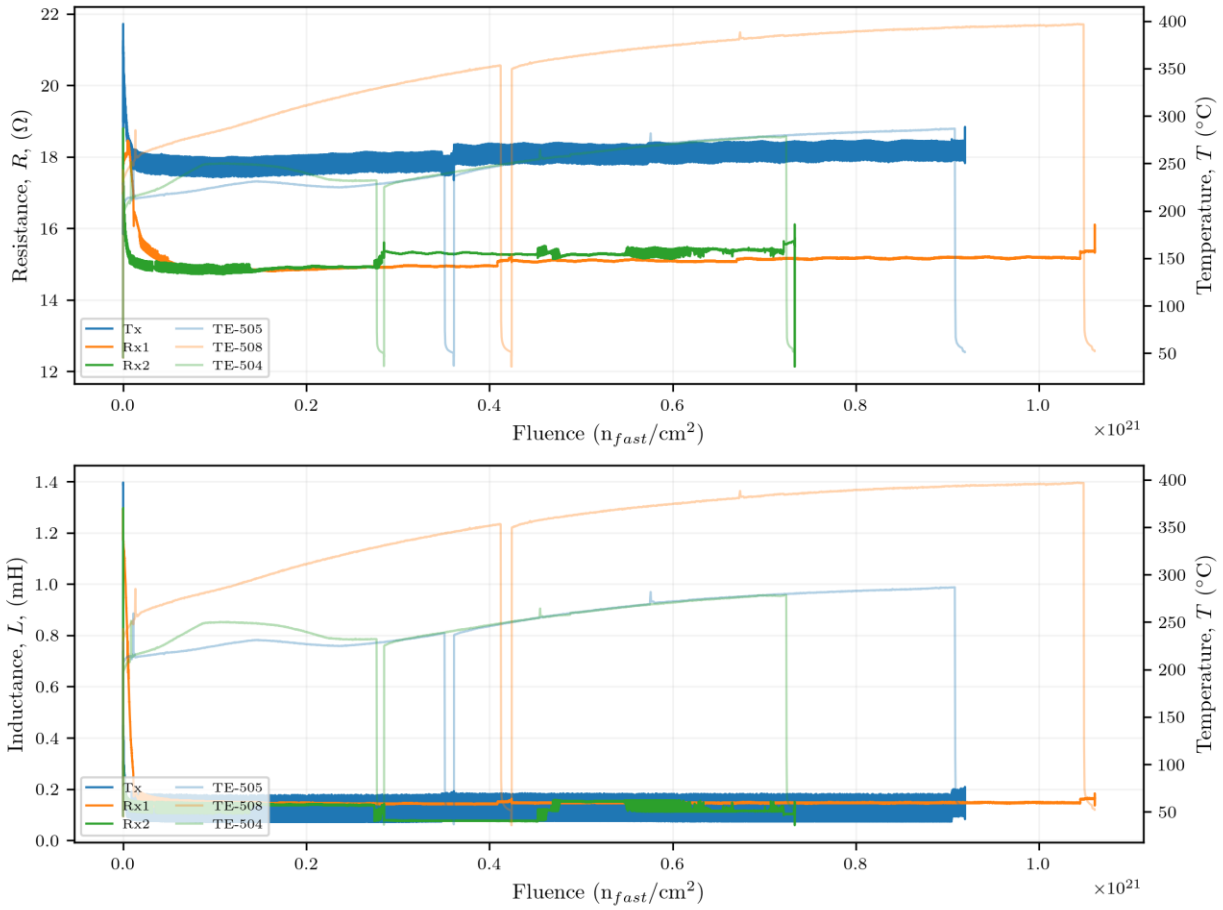

Figure 12. Change in the resistance (top) and inductance (bottom) of the three inductor circuits in WEC's temperature sensor vs. fast neutron fluence during cycle 498. The temperatures nearest each inductor (sensor IDs indicated in the figure legend) are also plotted on the right axes as a function of neutron fluence.

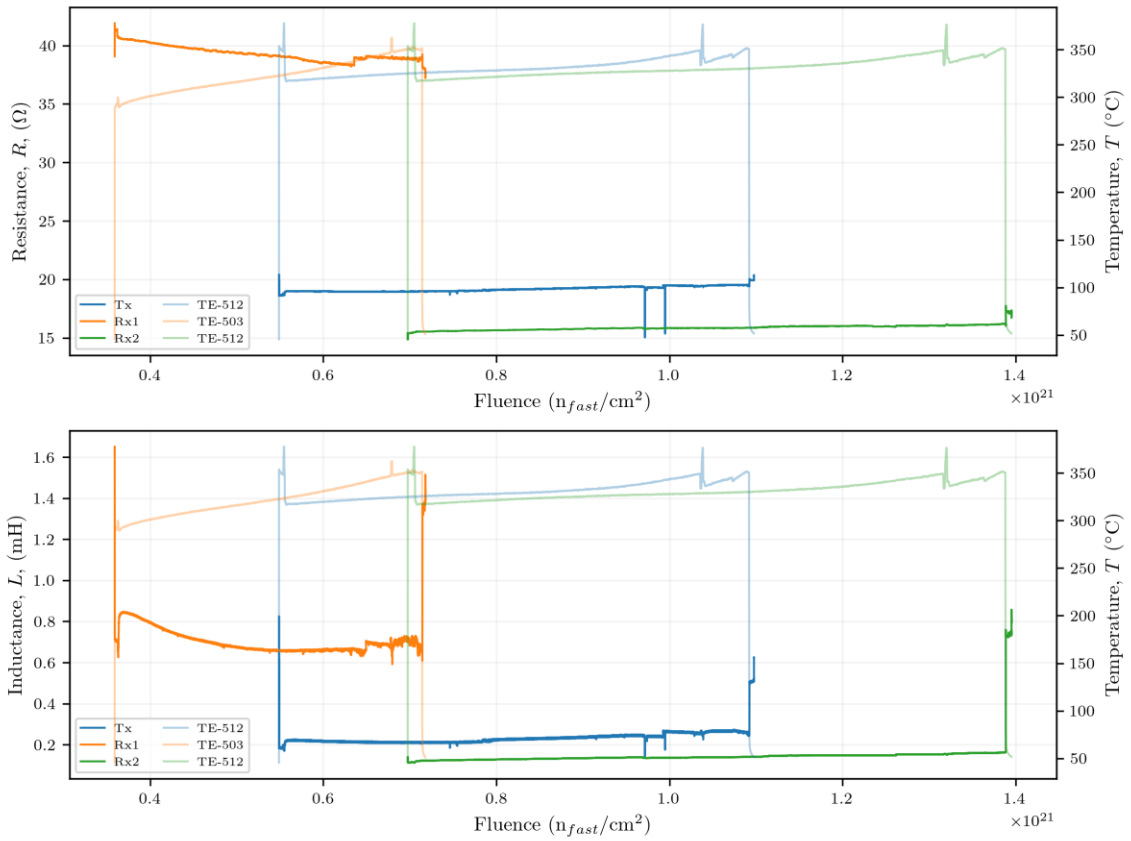

Figure 13. Change in the resistance (top) and inductance (bottom) of the three inductor circuits in WEC's pressure sensor vs. fast neutron fluence during cycle 499. The temperatures nearest each inductor (sensor IDs indicated in the figure legend) are also plotted on the right axes as a function of neutron fluence.

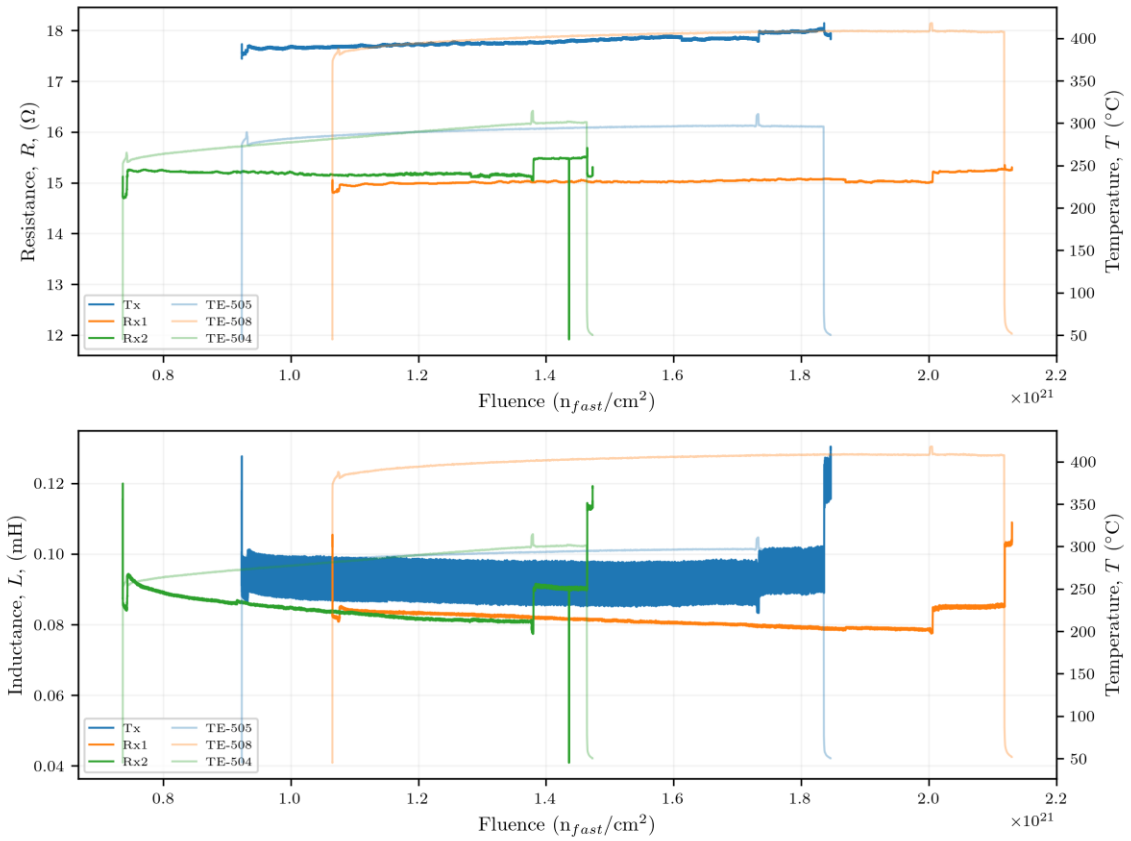

Figure 14. Change in the resistance (top) and inductance (bottom) of the three inductor circuits in WEC's temperature sensor vs. fast neutron fluence during cycle 499. The temperatures nearest each inductor (sensor IDs indicated in the figure legend) are also plotted on the right axes as a function of neutron fluence.

3.6 SPND RESPONSE

Four SPNDs manufactured by Idaho Laboratories Corporation were included in WIRE-21 for real-time neutron flux measurements of the experiment. The SPNDs used 5 cm lengths of high-purity vanadium wire as the emitter material, surrounded by MgO insulation and Inconel 600 sheathing. The emitter assembly was connected to a dual lead mineral insulated (MI) cable, composed of Inconel 600 electrical wires, MgO insulation, and Inconel 600 sheathing. The Inconel 600 wires were twisted inside the sheath to reduce electromagnetic interference, with approximately one rotation per foot. One lead from the MI cable was welded to the V emitter to extract the detector neutron response, whereas the second MI lead was left open to provide a gamma compensation signal along the cable length. The SPNDs were positioned at symmetrical elevations of 5 and 15 cm above and below the HFIR midplane, as shown in Figure 15.

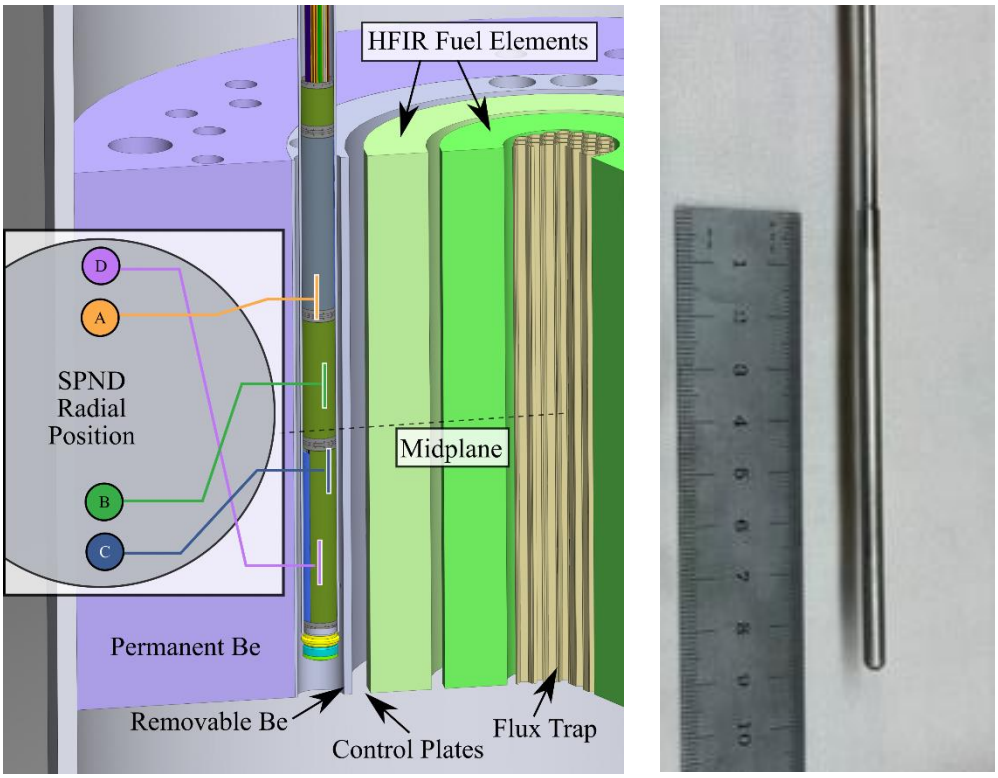

Figure 15. Locations of four SPNDs within WIRE-21 (left) and image of SPND prior to assembly (right).

Measurements were performed on each SPND before the first cycle of irradiation to verify the detectors' electrical characteristics, including their resistance, capacitance, and inductance, as shown in Table 3. Similar measurements will be performed in PIE to determine changes caused by neutron fluence accumulation or temperature effects.

Table 3. Pre-irradiation electrical measurements between the gamma compensation wires (γ), emitter wires (n), and collectors (n) of each SPND.

SPND	Resistance (Ω)			Capacitance (nF)			Inductance (mH)		
	γ to c	n to c	n to γ	γ to c	n to c	n to γ	γ to c	n to c	n to γ
-A	1.14	>1M	>1M	−20009	6.07	6.07	0.033	−4168	−4168
-B	2.25	>1M	>1M	−5900	6.04	6.04	0.033	−4192	−4192
-C	1.33	>1M	>1M	−15700	6.11	6.11	0.033	−4145	−4145
-D	1.16	>1M	>1M	−20001	6.18	6.18	0.033	−4099	−4099

Electrical current from the SPNDs was measured using a dual-channel 6482 Keithley picoammeter. SPNDs were electrically connected to data acquisition equipment in three different ways, one for each HFIR cycle, as summarized in Figure 16. During the first cycle of irradiation (498), the emitter of each SPND was connected to the input channel of a picoammeter, the gamma compensation wire was left floating, and the collector was signal grounded. For the second cycle of irradiation (499), the emitter and gamma compensation wire were connected to a custom preamplifier, described previously [5], whereas the collector was signal grounded. The preamplifier inverted the emitter signal before summing with the compensation signal. The output of the preamplifier corresponded, in theory, to the signal induced from only neutron interactions in the emitter wire. The cycle 500 configuration separately connected the emitter and compensation wires to input channels of the picoammeter while signal grounding the

collector. Due to physical limitations in cabling pathways between the reactor pool top and MIF, these connections were made to SPND-C and SPND-D only. Measurements from each cycle of irradiation are discussed in the following sections.

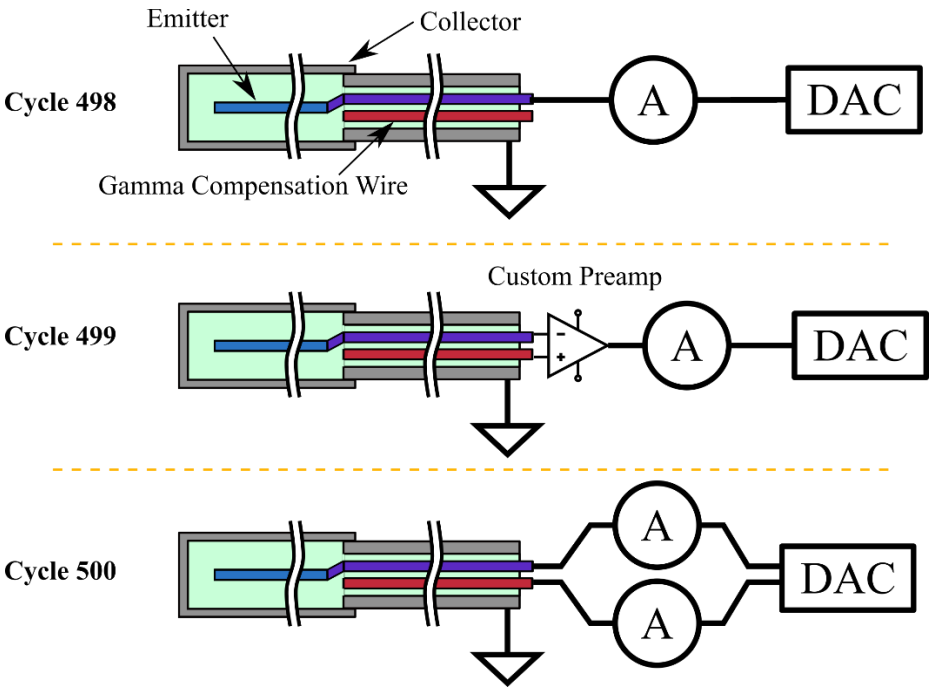

Figure 16. SPND electrical configurations for three cycles of irradiation.

3.6.1 Cycle 498 SPND Response

Signals from the emitter wire of each SPND for cycle 498, including the 6 d outage, are shown in Figure 17. The electrical current recorded in each SPND corresponds to neutron-induced beta decay in the V emitter, in combination with gamma or other neutron interactions along the length of the emitter wire. Other neutron interactions could include prompt or delayed beta emission from constituents of the wire or surrounding MgO insulation. As the figure shows, currents from SPND-A, -B, and -D clearly responded to changes in reactor power, though with different polarities. SPND-C also responded to changes in reactor power, though on a much smaller scale.

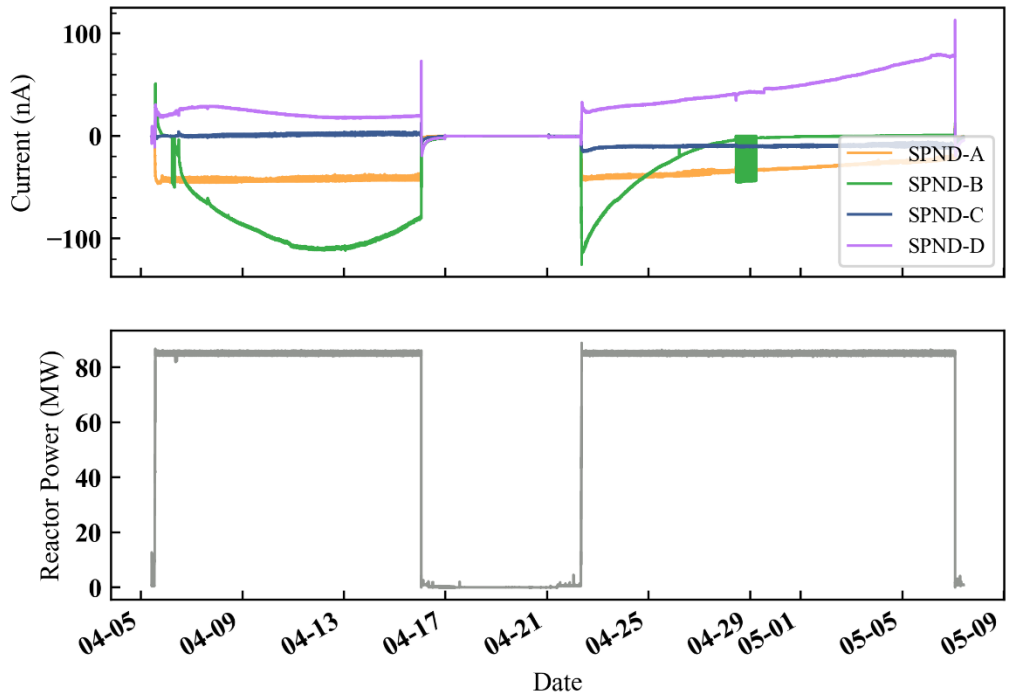

Figure 17. Electrical current from each SPND for cycle 498A and 498B (top), and HFIR reactor power (bottom).

Although it is difficult to discern at long time scales, 3 of the 4 SPNDs demonstrated a response to step changes in reactor power, which included short time scale (prompt gamma) and longer time scale (^{52}V beta decay) characteristics. Figure 18 focuses on the HFIR startup sequence, which included two steps in reactor power to 10 MW, followed by six power increases to 85 MW. Each increase in reactor power induced a prompt negative current, followed by an exponential increase in current with a half-life roughly equal to that of ^{52}V ($T_{1/2} = 224\ s$). Decreases in reactor power showed the inverse trend, with a prompt positive current followed by an exponential decrease with a half-life similar to ^{52}V. This result suggests a competing mechanism between prompt gamma contributions along the cabling and delayed beta emission in the emitter. Additional deconvolution of the time-varying SPND signal is planned for a future report.

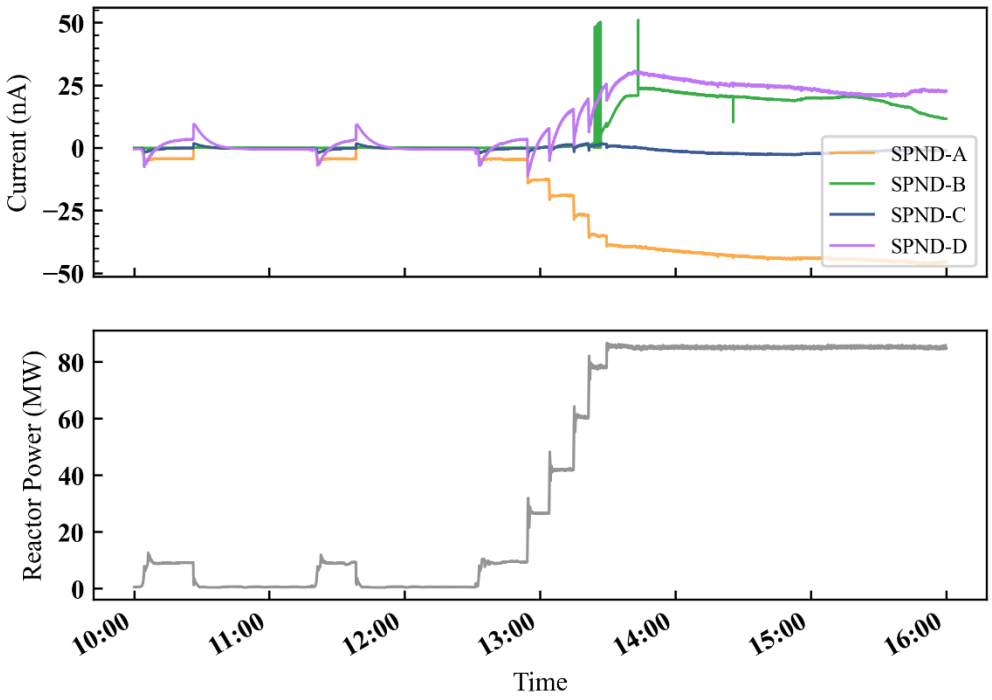

Figure 18. SPND signals during cycle 498A startup (top) and reactor power (bottom).

3.6.2 Cycle 499 SPND Response

SPNDs for cycle 499 were connected to a custom preamplifier, designed to subtract current of the gamma compensation wire from current in the emitter wire before measuring with the Keithley ammeter. The preamplifier was designed using an assumed gamma and neutron–induced current calculated from radiation transport modeling of the experiment and first-order estimates of the SPND's detection sensitivity. These calculations informed the selection of components and signal amplification in the custom preamplifier during the design phase of the experiment. Unfortunately, some of the assumptions relating to the SPND sensitivity and gamma contributions were inaccurate, resulting in a capped output signal between −5 nA and 5 nA, as shown in SPND-D and -B Figure 19. Additionally, due to the placement of the preamplifier in a junction box at the reactor pool top, gain adjustments could not be made during the HFIR cycle.

General trends in SPND behavior followed those observed in cycle 499, with SPND-D having the largest positive current and SPND-B having the largest negative current. SPND-C and -A generated electrical currents between these two extremes and provided clearer information regarding their response, although SPND-C suffered from signal chopping for the first several days of the cycle and intermittently near the end of cycle. SPND-A showed a noisy but resolvable response to changes in reactor power (Figure 20) with three increases in current for the initial three transients, followed by a steady ascent during the approach to full power. SPND-A and -C also showed an exponential decay in current following reactor shutdown (Figure 21), which indicates a signal response from delayed beta emission in ^{52}V. Additional analysis for SPNDs in this configuration is also planned for a future report, including a specific investigation of appropriate electrical gains for the preamplifiers.

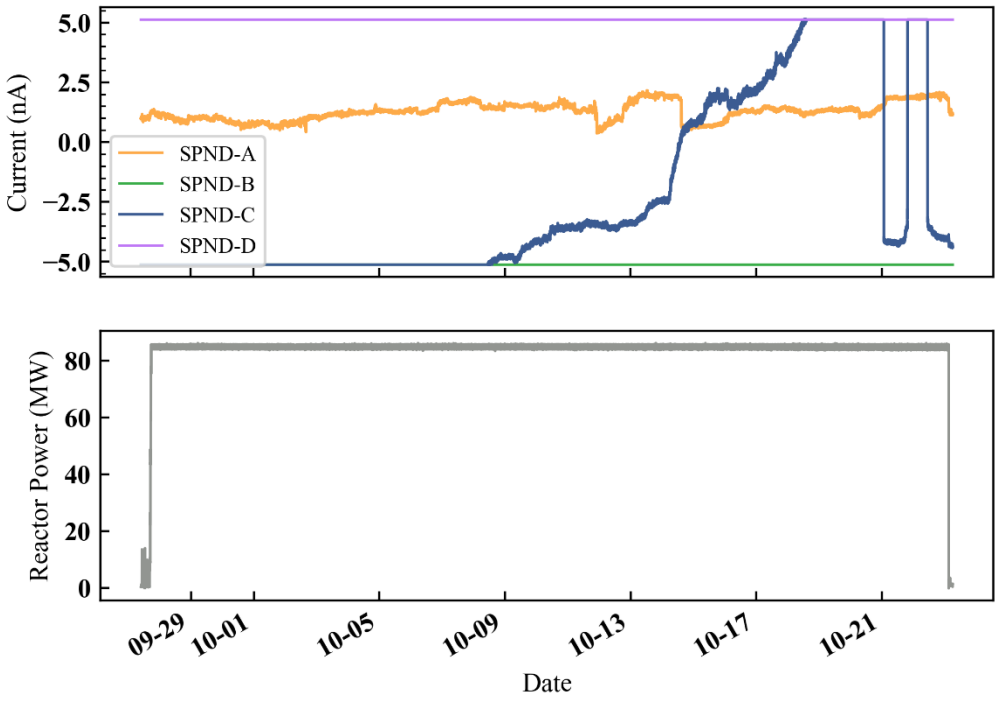

Figure 19. SPND signals during cycle 499 (top) and reactor power (bottom).

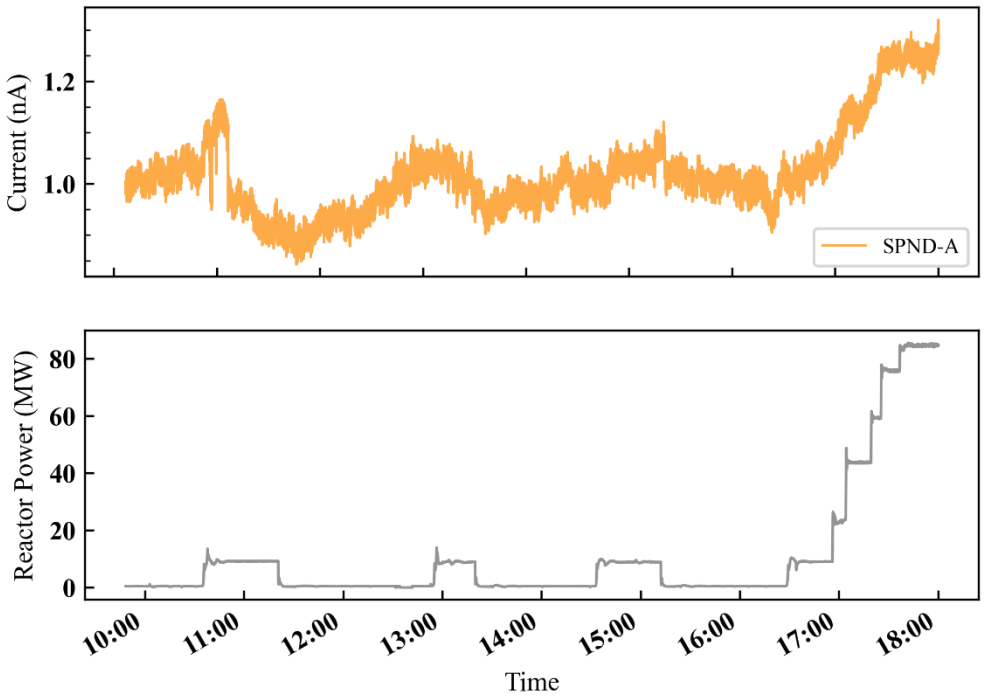

Figure 20. SPND-A response during cycle 499 startup operations.

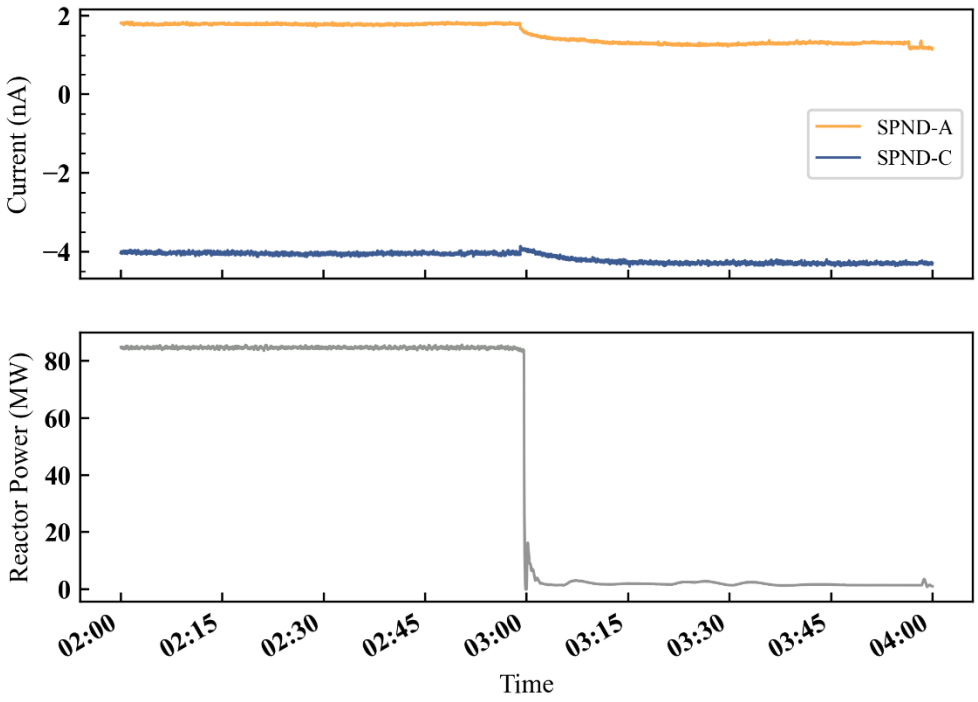

Figure 21. SPND-A and -C signal during reactor shutdown of cycle 499.

3.6.3 Cycle 500 SPND Response

For the final cycle of WIRE-21 irradiation, the electrical connections were reconfigured to separately record the emitter and gamma compensation current for SPND-C and -D. Unfortunately, SPND-D did not exhibit a response in either the emitter or gamma compensation wire, as shown in Figure 22. The source of this failure is unclear, as the detector seemed to be operating as expected during the first cycle of irradiation, but it will be investigated during PIE.

The emitter signal of SPND-C showed behavior similar to the SPND behavior in cycle 498, with a prompt negative current and subsequent exponential increase following each increase in power, as shown in Figure 23. The emitter wire current of SPND-C also showed a response to changes in reactor power, as shown in Figure 24, although with fewer resolvable transitions (2), compared to the larger number of power increases (6) during startup. The reason for this discrepancy is unknown. Reactor shutdown also produced an emitter response similar to that of cycle 498 (Figure 25), with a prompt increase in current followed by exponential decay with a ~224 s half-life. Further investigation of the SPND behavior, particularly of the gamma compensation current is planned for a future report.

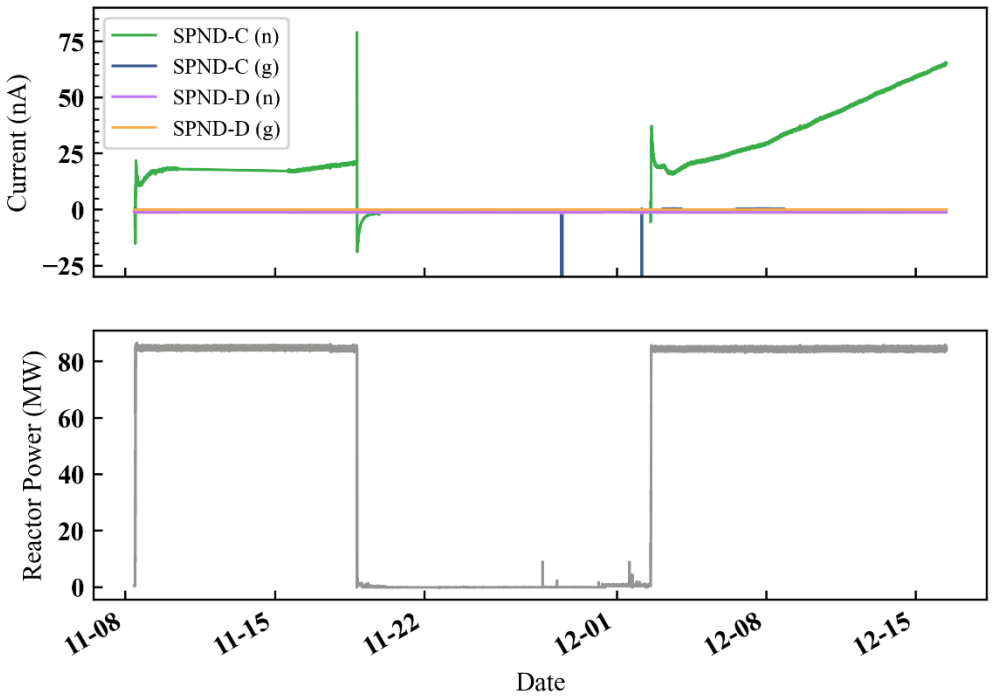

Figure 22. SPND-C and -D signals from emitter (n) and gamma compensation wire (g) during cycle 500.

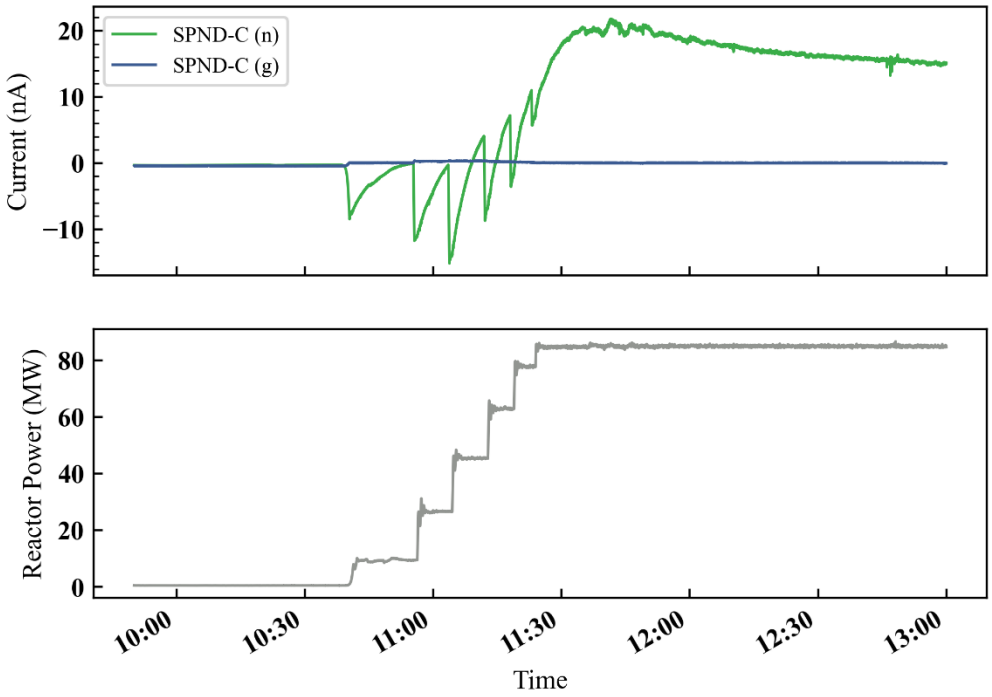

Figure 23. SPND-C signal from emitter (n) and gamma compensation wire (g) during startup of cycle 500.

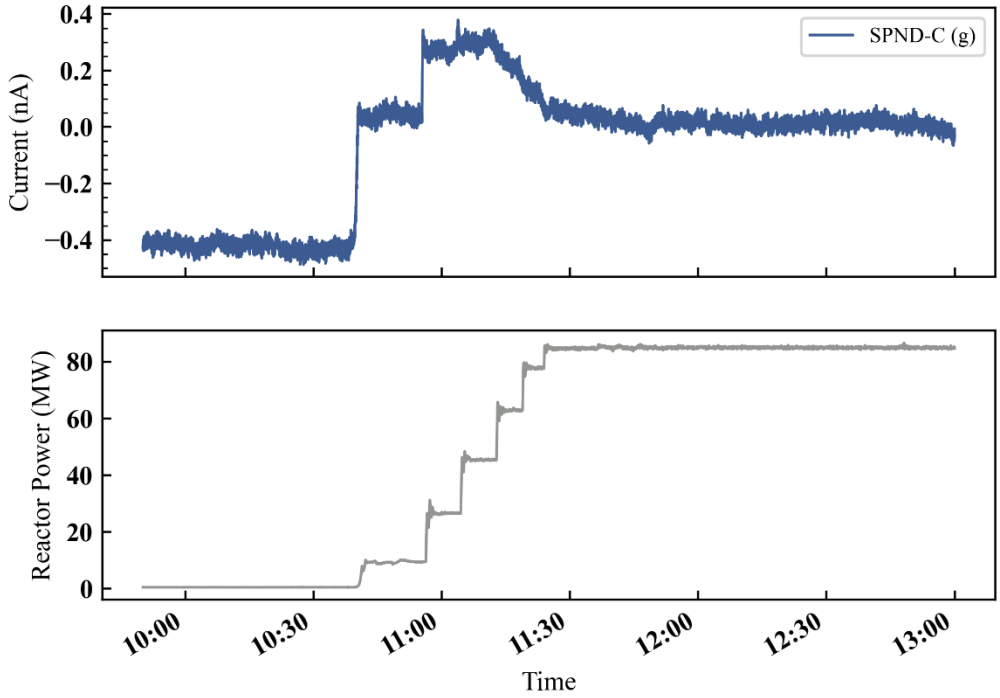

Figure 24. SPND-C gamma compensation signal during cycle 500 startup.

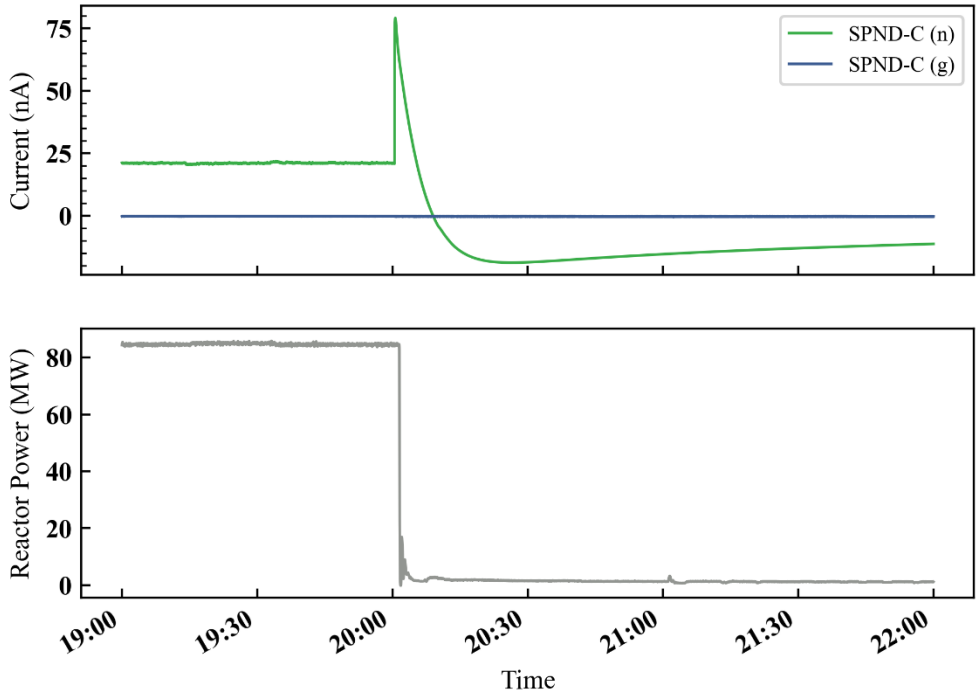

Figure 25. SPND-C signal during cycle 500A scram event.

3.7 OPTICAL FIBER SENSOR RESPONSE

Data were acquired in situ from eight fiber optic sensors with and without inscribed Bragg gratings, as described in more detail in a previous report [5]. Both Type I and Type II gratings were included in the test. Type I gratings are written with an ultraviolet laser in photosensitive fibers, whereas Type II gratings are inscribed with a femtosecond laser. In addition to varying the grating type, various fiber compositions were also tested, including fibers with a pure silica core and F-doped silica cladding as well as fibers with a Ge-doped silica core and a pure silica cladding. Finally, hollow core fibers were included that rely on a photonic bandgap instead of total internal reflection to confine the light signal. Because light is not guided within a solid material, hollow core fibers could be more tolerant to radiation as demonstrated during initial irradiation testing performed previously by others [8].

All fibers were interrogated using near-infrared (~1550 nm wavelength) optical backscatter reflectometry (OBR) using the 4600 model from Luna Innovations. This provides information on the backscattered light amplitude as a function of position along the length of the fiber. In addition, Fourier analysis allows for determination of local spectral shifts that are calibrated to changes in temperature to allow for spatially distributed temperature sensing [9]. The latter process requires significant effort to analyze the ~terabytes of generated data, especially considering that adaptive reference techniques [10-12] are required to resolve fiber spectral shifts when the backscatter profile dynamically changes under intense neutron irradiation. The Advanced Sensors and Instrumentation (ASI) program, within the US Department of Energy, Office of Nuclear Energy (DOE-NE), is interested in these data and is currently funding analysis and interpretation to inform the future direction of fiber optic sensing within the ASI program. Therefore, this report describes only briefly the high-level observations obtained from the initial analysis of the reflected signal amplitudes from the fiber optic sensors. Figure 26 shows the reflected signal amplitude, or intensity, versus position relative to the reactor midplane for the two fibers without FBGs that rely on total internal reflection to confine the light signals. Results are shown prior to irradiation and at various BOC, middle of cycle (MOC), and EOC times. The EFPDs are also indicated in the figure legend. One fiber (CH01) was composed of a pure silica core and F-doped silica cladding. The other fiber (CH02) was composed of a Ge-doped silica core and a pure silica cladding. In the initial scans, both fibers show two peaks corresponding to the end of the fiber assembly (left peaks) and the splice from the sensing fiber to a coreless termination fiber (right peaks). During the first cycle of irradiation, a broad peak develops that moves to the right with increasing time throughout the cycle. As described in more detail elsewhere [13], this peak is caused by Fresnel reflections that develop as the glass compacts under irradiation. At a sufficiently high neutron fluence, the compaction reaches an equilibrium, which eliminates the reflections near the core midplane. However, the effects of Fresnel reflections can still be seen farther above the core, where the neutron fluence is lower and the compaction has not yet saturated.

The effects of Fresnel reflections are not as obvious for CH02 because this fiber clearly suffers from significant light attenuation, as evidenced by the intensities being reduced to the noise floor (approximately −142 dB) by the end of the first cycle, for positions within 40 cm of the core midplane. In contrast, CH01 does shows no evidence of significant attenuation at the end of the first cycle. In fact, the intensities remain higher than pre-irradiation values at this point. This is due to the difference in the fiber dopants (F vs. Ge). Unfortunately, the CH01 fiber was broken in the experiment junction box located in the reactor pool area during the outage after the first irradiation cycle.

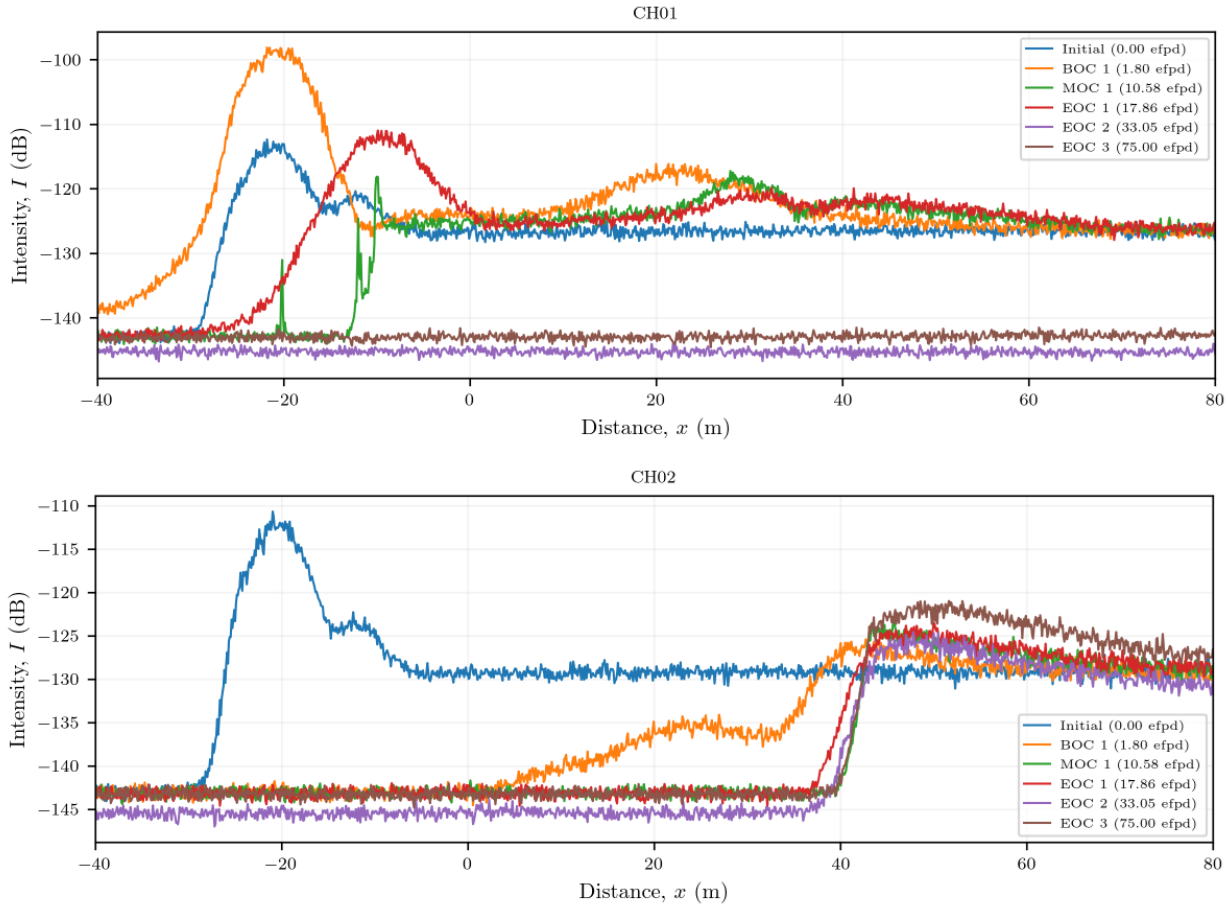

Figure 26. Backscattered light intensity vs. position for a pure silica core, F-doped silica fiber (CH01) and a Ge-doped silica core, pure silica cladding fiber (CH02), both without FBGs.

Figure 27 shows the reflected signal intensity vs. position relative to the reactor midplane for two fibers with a F-doped silica core and cladding (higher doping in the cladding) and inscribed Type II FBGs. Initially, the grating regions are somewhat visible between approximately −10 cm and +50 cm (CH03) or +30 cm (CH04); however, the individual FBGs are not easily discernable. The FBGs are more visible at MOC 1 and EOC 3. These scans were taken when the reactor and coolant pumps were not operating. Therefore, it is likely that the vibrations caused by operation of the reactor and coolant pumps affected the visibility of the FBGs. The increased visibility after cycle 3 could also be related to the fact that signal attenuators were removed after cycle 2. These attenuators prevented the detectors from saturating early in the experiment. After the signals became weaker due to radiation-induced attenuation in the fiber and/or gratings, the attenuators were able to be removed without saturating the detectors.

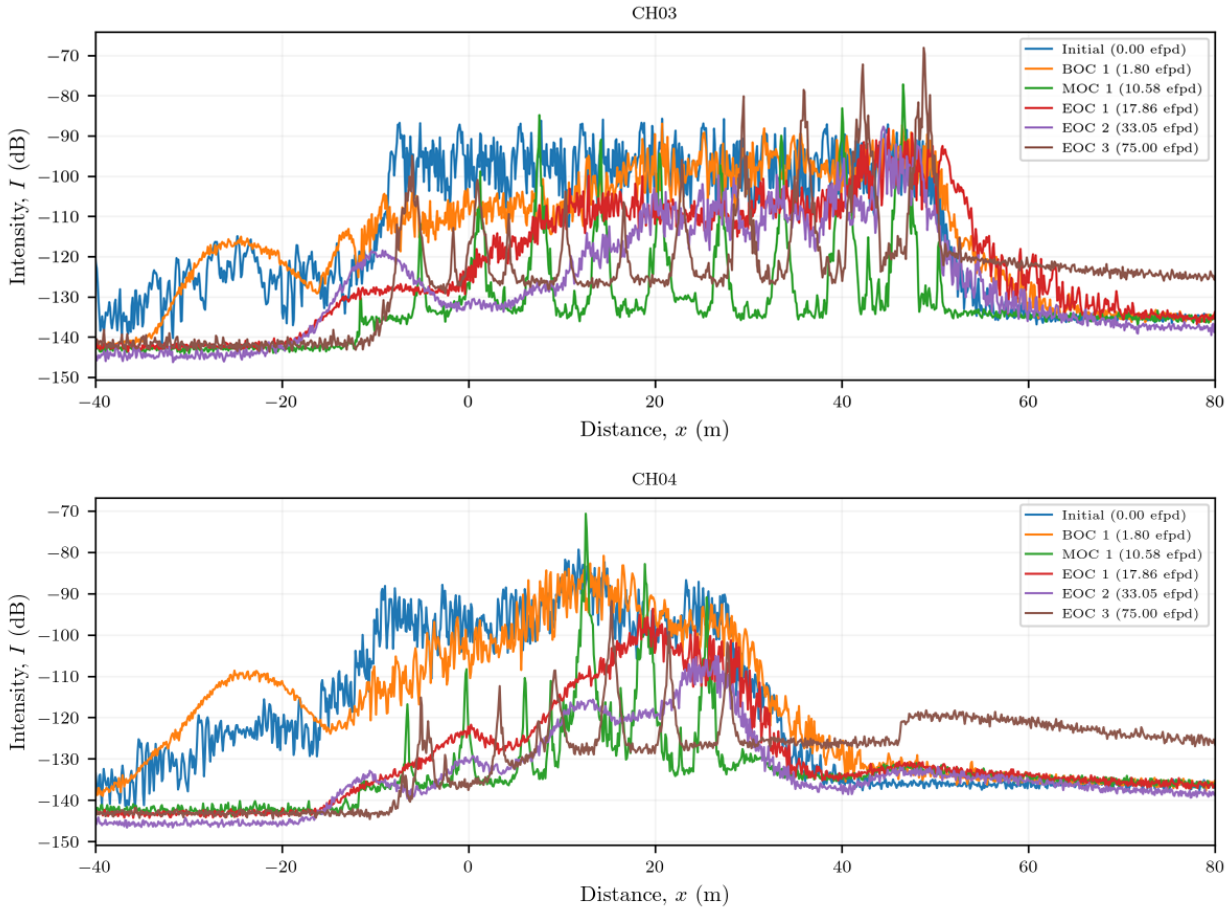

Figure 27. Backscattered light intensity vs. position for two fibers with F-doped silica core and cladding with varying numbers of inscribed Type II FBGs.

Figure 28 shows the reflected signal intensity vs. position relative to the reactor midplane for two fibers with different types of dopants and FBGs. One fiber (CH05) has a pure silica core, F-doped silica cladding (same as CH01) with inscribed Type II FBGs. The other (CH06) has a Ge-doped silica core and pure silica cladding (similar to CH02) with inscribed Type I FBGs. Similar to CH03 and CH04, it is difficult to identify individual FBGs in CH05, except at MOC 1 and EOC 3. However, the FBGs in CH05 appear to be attenuated more significantly compared with those from CH03 and CH04. This could be related to the increased F doping in the CH03 and CH04 fibers.

CH06 has a much higher grating density, so individual gratings cannot be resolved in any of the scans. By MOC 1, the intensities in the CH06 fiber approach values close to −120 dB, which is similar to those of CH01, which does not contain FBGs. Interestingly, despite the CH06 fiber having a Ge-doped core that is expected to suffer from radiation-induced attenuation (see CH02), the fiber appears to maintain intensities close to −120 dB at positions 15–20 cm above the core. For comparison, the region upstream of the FBGs showed reflected intensities close to −125 dB. Therefore, despite the FBG intensities decreasing, the intensities remain higher than those from Rayleigh backscatter, indicating that the gratings in the CH06 fiber are providing some benefit relative to the non-grating region. It is not quite clear why the intensities at EOC 2 are lower than those at EOC 3 for all positions, even those downstream of the fiber termination.

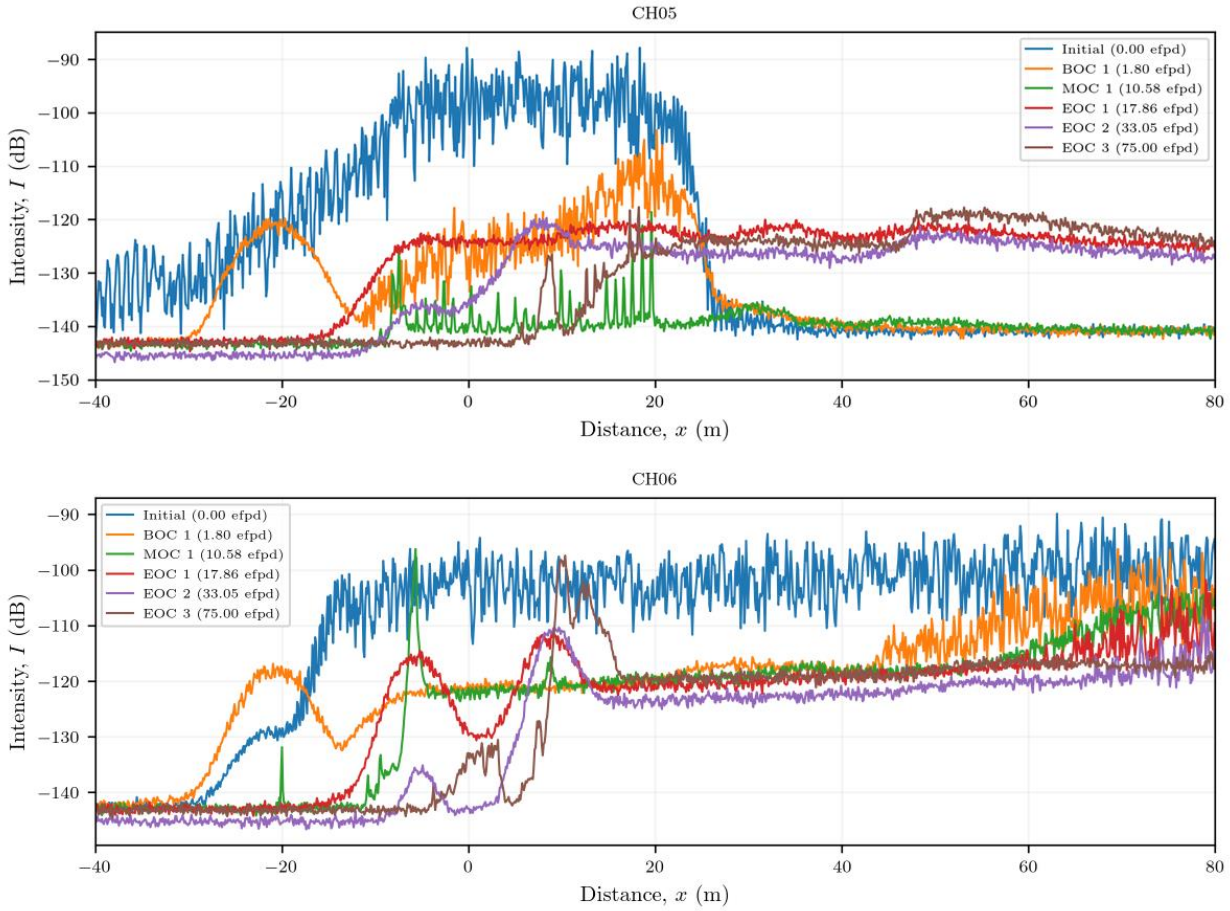

Figure 28. Backscattered light intensity vs. position for a pure silica core, F-doped silica fiber with Type II FBGs (CH05) and a Ge-doped silica core, pure silica cladding fiber with Type I FBGs (CH06).

Figure 29 shows the reflected signal intensity vs. position relative to the reactor midplane for two hollow core fibers without inscribed FBGs. The figure caption describes the locations of the splices from pure silica core, F-doped silica cladding fibers to the hollow core fiber section. These data are more difficult to interpret. CH07 shows minimal changes in the intensities within the hollow core region between 25–50 cm. There are some increased reflections near 15 cm with decreased intensities moving to lower positions. CH08 shows a different behavior, with intensities decreasing over the entire length of the hollow core region. After 3 cycles, the intensities approach the system noise floor for all positions below ~30 cm. More analysis of this data will be required to determine the discrepancies between these two hollow core fibers.

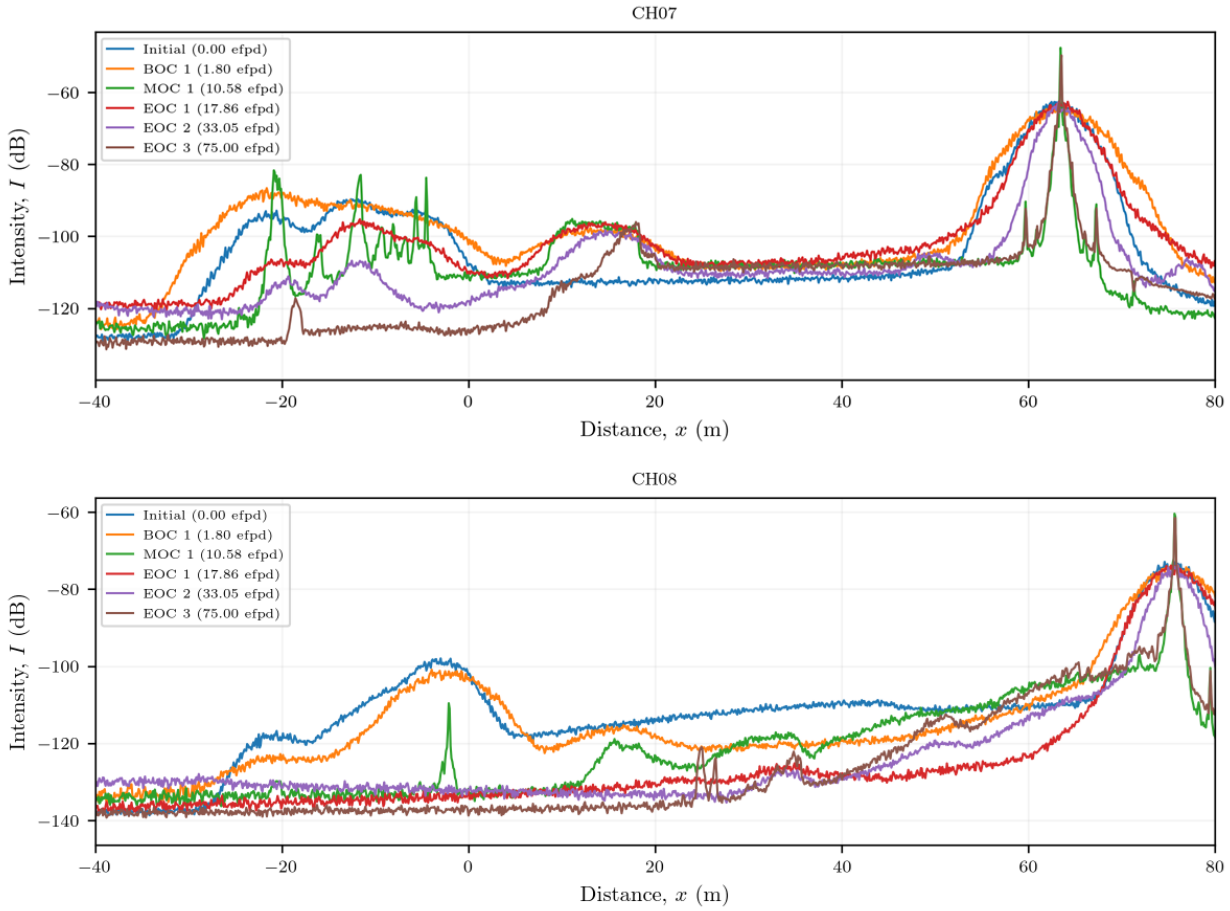

Figure 29. Backscattered light intensity vs. position for two hollow core fibers without inscribed FBGs. The large peaks between 60 and 80 cm are the splices from a pure silica core, F-doped silica cladding fiber (right side) to the ~1.2 m long hollow core fiber (left side). Additional ~15 cm long sections of pure silica core, F-doped silica cladding fiber were spliced to the opposite ends of the hollow core fibers. Peaks corresponding to those splices can be seen near −5 to 0 cm. The distances within the hollow core fiber region are not accurate because the refractive index in the hollow core (~1) is different than that in the solid core fibers (~1.44).

4. PLANNED POST-IRRADAITION EXAMINATION

The primary goal of this experiment was to collect in situ data during irradiation from WEC's wireless sensors. Having completed the irradiation testing, focus will now shift to PIE. The extent of PIE that will be conducted will depend on the funding that remains after shipment and disassembly. The following list, presented generally in order of priority, summarizes planned PIE:

- extraction of WEC sensors,
- visual examinations of the interior and exterior of WEC's sensor enclosures,
- extraction of passive TMs and flux wires,
- measurements of local inductances and resistances inside WEC's sensor enclosures,
- extraction of fiber samples and SPND emitters to make available to the NSUF material library,
- dilatometric analysis of TMs, and
- gamma spectroscopy of flux wires.

5. FUTURE DATA ANALYSIS

In addition to completing PIE, many activities are being considered for future publications, some of which may require follow-on funding. These include

- comparison of experiment thermal models with measured temperatures from thermocouples, fiber optic sensors, WEC's sensors, and passive TMs,
- comparison of post-irradiation analysis techniques for evaluating passive TMs used by ORNL, Idaho National Laboratory, and potentially other organizations,
- comparison of neutronic models with measured data from SPNDs and flux wires,
- analysis of fiber optic signal degradation and drift, and
- evaluation of fundamental degradation mechanisms in WEC's inductors.

6. REFERENCES

1. K. A. Terrani et al., "Accelerating nuclear fuel development and qualification: Modeling and simulation integrated with separate-effects testing," *Journal of Nuclear Materials* 539 (2020) 152267.
2. J. V. Carvajal et al., "Nuclear Radiation–Tolerant Wireless Transmitter Irradiation Test Results," *Nuclear Technology* 197 (2017) 201–208.
3. J. Carvajal et al., "Integral Fuel Rod Real-Time Wireless Sensor," in *11th International Conference On Nuclear Plant Instrumentation, Control, and Human-Machine Interface Technologies* Orlando, FL (2019) 1000–1012.
4. P. L. Mulligan et al., *Wireless Instrumented RB Experiment Preliminary Design and Analysis*, ORNL/TM-2020/1879, Oak Ridge National Laboratory, Oak Ridge, TN (2020).
5. C. Petrie et al., *WIRE-21 Sensor Irradiation Experiment Ready for HFIR Insertion*, ORNL/TM-2022/2354, Oak Ridge National Laboratory, Oak Ridge, TN (2022).
6. P. L. Mulligan et al., "In-Core Neutron Flux, Temperature, and Pressure Instrumentation for the WIRE-21 Experiment in the High Flux Isotope Reactor," in *12th Nuclear Plant Instrumentation, Control and Human-Machine Interface Technologies*, United States (2021) 564-574.
7. K. G. Field et al., "Evaluation of the continuous dilatometer method of silicon carbide thermometry for passive irradiation temperature determination," *Nuclear Instruments and Methods in Physics Research Section B: Beam Interactions with Materials and Atoms* 445 (2019) 46–56.
8. G. Cheymol et al., "High Level Gamma and Neutron Irradiation of Silica Optical Fibers in CEA OSIRIS Nuclear Reactor," *IEEE Transactions on Nuclear Science* 55 (2008) 2252–2258.
9. M. Froggatt and J. Moore, "High-spatial-resolution distributed strain measurement in optical fiber with Rayleigh scatter," *Applied Optics* 37 (1998) 1735–1740.
10. D. C. Sweeney, A. M. Schrell, and C. M. Petrie, "An Adaptive Reference Scheme to Extend the Functional Range of Optical Backscatter Reflectometry in Extreme Environments," *IEEE Sensors Journal* 21 (2020) 498–509.
11. D. C. Sweeney, D. M. Sweeney, and C. M. Petrie, "Graphical Optimization of Spectral Shift Reconstructions for Optical Backscatter Reflectometry," *Sensors* 21 (2021) 6154.
12. D. C. Sweeney and C. M. Petrie, "Expanding the range of the resolvable strain from distributed fiber optic sensors using a local adaptive reference approach," *Optics Letters* 47 (2022) 269-272.
13. C. M. Petrie and D. C. Sweeney, "Enhanced backscatter and unsaturated blue wavelength shifts in F-doped fused silica optical fibers exposed to extreme neutron radiation damage," *Journal of Non-Crystalline Solids* (under review).